Monthly Notices
of the
ROYAL ASTRONOMICAL SOCIETY

Mon. Not. R. Astron. Soc. **424,** 2232–2248 (2012) doi:10.1111/j.1365-2966.2012.21386.x

Integral field spectroscopy of $2.0 < z < 2.7$ submillimetre galaxies: gas morphologies and kinematics

S. Alaghband-Zadeh,[1⋆] S. C. Chapman,[1] A. M. Swinbank,[2] Ian Smail,[2] C. M. Harrison,[3] D. M. Alexander,[3] C. M. Casey,[4] R. Davé,[5] D. Narayanan,[5] Y. Tamura[6] and H. Umehata[6]

[1]*Institute of Astronomy, Madingley Road, Cambridge CB3 0HA*
[2]*Institute for Computational Cosmology, Durham University, South Road, Durham DH1 3LE*
[3]*Department of Physics, Durham University, South Road, Durham DH1 3LE*
[4]*Institute for Astronomy, 2680 Woodlawn Dr, Honolulu, HI 96822, USA*
[5]*Astronomy Department, University of Arizona, Tucson, AZ 85721, USA*
[6]*Institute of Astronomy, The University of Tokyo, 2-21-1 Osawa, Mitaka, Tokyo 181-0015, Japan*

Accepted 2012 May 24. Received 2012 May 22; in original form 2012 March 31

ABSTRACT

We present 2D, integral field spectroscopy covering the rest-frame wavelengths of strong optical emission lines in nine submillimetre luminous galaxies (SMGs) at $2.0 < z < 2.7$. The Gemini-North/Near-Infrared Integral Field Spectrograph (NIFS) and Very Large Telescope (VLT) Spectrograph for INtegral Field Observations in the Near Infrared (SINFONI) imaging spectroscopy allow the mapping of the gas morphologies and dynamics within the sources, and we measure an average Hα velocity dispersion of $\langle\sigma\rangle = 220 \pm 80\,\mathrm{km\,s^{-1}}$ and an average half-light radius of $\langle r_{1/2}\rangle = 3.7 \pm 0.8\,\mathrm{kpc}$. The dynamical measure, $\langle V_{\rm obs}/2\sigma\rangle = 0.9 \pm 0.1$, for the SMGs is higher than in more quiescent star-forming galaxies at the same redshift, highlighting a difference in the dynamics of the two populations. The far-infrared star formation rates (SFRs) of the SMGs, measured using *Herschel*-SPIRE[†] far-infrared photometry, are on average $370 \pm 90\,\mathrm{M_\odot\,yr^{-1}}$, which is ∼2 times higher than the extinction-corrected SFRs of the more quiescent star-forming galaxies. Six of the SMGs in our sample show strong evidence for kinematically distinct multiple components with average velocity offsets of $200 \pm 100\,\mathrm{km\,s^{-1}}$ and average projected spatial offsets of $8 \pm 2\,\mathrm{kpc}$, which we attribute to systems in the early stages of major mergers. Indeed, all SMGs are classified as mergers from a kinemetry analysis of the velocity and dispersion field asymmetry. We bring together our sample with the seven other SMGs with integral field unit observations to describe the ionized gas morphologies and kinematics in a sample of 16 SMGs. By comparing the velocity and spatial offsets of the SMG Hα components with subhalo offsets in the Millennium Simulation data base, we infer an average halo mass for SMGs in the range of $13 < \log(M[h^{-1}\,\mathrm{M_\odot}]) < 14$. Finally, we explore the relationship between the velocity dispersion and star formation intensity within the SMGs, finding that the gas motions are consistent with the Kennicutt–Schmidt law and a range of extinction corrections, although they might also be driven by the tidal torques from merging or even the star formation itself.

Key words: galaxies: evolution – galaxies: high-redshift – galaxies: kinematics and dynamics – galaxies: starburst – galaxies: star formation.

⋆E-mail: sa543@cam.ac.uk

[†]*Herschel* is an ESA space observatory with science instruments provided by European-led Principal Investigator consortia and with important participation from NASA.

1 INTRODUCTION

Studies of the Hα nebular emission line have revolutionized our understanding of moderate-luminosity star-forming galaxies at $z \sim 2$. The most extensive study to date has been through the Spectroscopic Imaging survey in the Near-infrared with SINFONI (SINS) of 62 star-forming galaxies at $1.3 < z < 2.6$ (Förster-Schreiber et al. 2009), a subset of known Hα emitters from the ultraviolet (UV) continuum-selected galaxies (Daddi et al. 2004; Steidel et al. 2004). In the SINS galaxies, the Hα velocity fields are mapped to trace the dynamics of the ionized gas within the galaxies, with a striking result that the star-forming galaxies can be split into three equally populated groups: turbulent discs which are rotation dominated, compact sources which are dispersion dominated and merging systems. These galaxies populate the 'main sequence' of star-forming galaxies at these redshifts (e.g. Daddi et al. 2007; Noeske et al. 2007). The SINS survey, however, has only 6 per cent of galaxies with inferred star formation rates (SFRs) greater than 500 $M_\odot$ yr^{-1}, which is the domain of galaxies selected through bright far-infrared emission redshifted into the submillimetre (submm) wavelengths or submm galaxies (SMGs). Further, the poorly constrained dust extinction corrections in the SINS galaxies implies that this 'high-SFR' tail may actually have substantially lower SFRs. There is thus an obvious need to explore the nebular emission-line dynamics of the SMG population to compare to the 'main sequence' of star-forming galaxies.

Since their discovery, SMGs have been the focus of intense multi-wavelength study. With 15 years since the first submm surveys (e.g. Smail, Ivison & Blain 1997; Hughes et al. 1998) our understanding of this population has grown considerably, although still limited by only handfuls of objects studied in detail at high spatial resolution (e.g. Swinbank et al. 2006; Carilli et al. 2010; Engel et al. 2010). These dusty galaxies have a redshift distribution which peaks at $z \sim 2.5$ (Chapman et al. 2005; Wardlow et al. 2011). At these redshifts, the observed submm flux densities imply far-infrared luminosities $>10^{12}$ $L_\odot$ (ultraluminous infrared galaxies: ULIRGs). With space densities at $z \sim 2$ a factor of $\sim$1000 times higher than today (Chapman et al. 2003), these luminous systems contribute $\sim$30 per cent of the star formation activity at $z \sim 2$–3, compared to $<$1 per cent locally. It is noteworthy that some confirmed ULIRGs at $z \sim 2$ have hotter spectral energy distribution (SED) shapes, resulting in 850-μm fluxes lying below the sensitivities of current surveys, and the high-redshift ULIRG population could be up to twice as large as implied by 850-μm surveys alone (Chapman et al. 2004c; Casey et al. 2009; Magdis et al. 2010). These galaxies which have been missed by 850-μm surveys have been detected by *BLAST* (Casey et al. 2011) and *Herschel* (Magnelli et al. 2010; Chapman et al. 2010), and confirmed as 'SMGs' with 250–500 μm flux densities still implying ULIRG-like luminosities. The intense SFRs ($\sim$1000 $M_\odot$ yr^{-1}) and large molecular gas reservoirs ($\sim 10^{11}$ $M_\odot$; Greve et al. 2005; Bothwell et al. 2012) inferred for the SMGs means that they could build a stellar mass of 10^{11} $M_\odot$ in just 100 Myr. The space densities and inferred duty cycles of SMGs suggest they represent the formation phase of today's massive elliptical galaxies (Lilly et al. 1999; Genzel et al. 2003; Swinbank et al. 2008).

SMGs are clearly an influential population of early galaxy evolution, but attempts to model their basic properties have proved problematic. The most successful semi-analytic models have had to radically alter their prescriptions for starbursts during mergers in order to account for SMGs whilst remaining self-consistent with other constraints (Baugh et al. 2005). Narayanan et al. (2009) looked at isolated conditions in hydrodynamical simulations that could lead to very high SFRs, and proposed a merger-driven formation scenario for SMGs. Subsequent analysis by Hayward et al. (2011b) showed that these merging galaxies may represent the bright end of the SMG number counts, but found that the fainter tail of SMGs ($S_{850} \sim 3$ mJy) are typically made up of isolated galaxies and galaxy pairs. Davé et al. (2010) identified SMGs in their cosmological simulations as typically very massive galaxies which are being harassed by small fragments, offering an alternative possibility to the major-merger picture for SMGs. Observations of individual SMGs at high resolution are therefore required to guide the models and constrain the driver for the high SFRs.

High-resolution radio and CO observations have shown that the star formation and gas can be extended on scales up to $\sim$10 kpc in SMGs, and multiple components are common within these extended distributions (Chapman et al. 2004b; Biggs & Ivison 2008; Tacconi et al. 2008; Casey et al. 2009; Bothwell et al. 2010; Ivison et al. 2011). These sizes are much larger than the typical $\sim$1 kpc extent of local ULIRGs (e.g. Sakamoto et al. 2008) whose intense SFRs are often triggered by mergers and interactions (Sanders & Mirabel 1996). Engel et al. (2010) and Bothwell et al. (2010) concluded that most SMGs are formed in major mergers, many exhibiting distinct kinematic components and disturbed gas morphologies (indicative of pre-coalesced to late stage mergers) from their high-resolution interferometric CO line studies.

Studying SMGs in Hα complements the CO studies, as lower levels of star formation are detectable through Hα emission rather than through the existing CO or radio measurements [from the institut de radioastronomie millimétrique (IRAM) Plateau de Bure Interferometer and the Very Large Array (VLA), respectively]. Further, merging galaxies may not induce similarly high levels of star formation in all components of the merger, and Hα may elucidate a more extensive merging system than apparent in CO. Swinbank et al. (2006) find multiple components in four of the six SMGs they studied using integral field unit (IFU) spectroscopy to map Hα, with average velocity offsets of $\sim$180 km s^{-1} and spatial offsets up to $\sim$8 kpc. They concluded that SMGs are similar to the local, more compact ULIRGs in that they exhibit multiple components. However, they were not able to resolve kinematic information on scales $<$5 kpc (i.e. within each component), and thus the gas dynamics of the multicomponent systems could not be established. Using higher spatial resolution IFU observations, Menendez-Delmestre et al. (in preparation) measure the gas kinematics within the multiple components of three SMGs. However, the majority of the Hα fields of these three sources are dominated by broad-line active galactic nuclei (AGN), and only small sections of the narrow-line regions have [N II]/Hα ratios which are consistent with photoionization from star formation. There has thus remained a need to further explore a larger sample of SMGs with high-resolution, sensitive IFU spectroscopy, including the large fraction of SMGs ($>$50 per cent) which do not show such obvious indications of strong AGN in their optical spectra.

In this paper we present the gas dynamics of nine SMGs observed with the Gemini-North/Near-Infrared Integral Field Spectrograph (NIFS) and Very Large Telescope (VLT) Spectrograph for INtegral Field Observations in the Near Infrared (SINFONI). In Section 2 we present the sample and the observations. In Section 3 we analyse the spatially integrated and resolved observations. The dynamical properties of the SMGs are presented in Section 4 along with the comparison to other galaxy surveys and the kinemetry analysis. In Section 5 we discuss the merger properties and use the component properties to infer the average halo mass. Finally, in Section 6 we give our main conclusions. All calculations assume a flat, Λ

Table 1. Table of the SMG fluxes, positions, redshifts and on-source exposure times. The redshifts quoted are derived from the IFU spectra measurements of the Hα emission line. The values in parentheses in the redshift column represent the error on the last decimal place. The radio flux and position references are given in the final column. The $S_{250\,\mu m}$, $S_{350\,\mu m}$ and $S_{500\,\mu m}$ fluxes are measured from *Herschel*-SPIRE observations (Griffin et al. 2010; Oliver et al. 2012). The errors quoted are the source extraction errors, but we note that these are dominated by the confusion noise (5.8, 6.3 and 6.8 mJy beam^{-1} for $S_{250\,\mu m}$, $S_{350\,\mu m}$ and $S_{500\,\mu m}$, respectively). The $S_{850\,\mu m}$ fluxes are taken from Chapman et al. (2005), Coppin et al. (2006) and Weiß et al. (2009).

Source	RA (J2000)	Dec. (J2000)	$z_{H\alpha}$	$S_{1.4\,GHz}$ (μJy)	$S_{250\,\mu m}$ (mJy)	$S_{350\,\mu m}$ (mJy)	$S_{500\,\mu m}$ (mJy)	$S_{850\,\mu m}$ (mJy)	t_{int} (ks)	Notes
RG J0331−2739[a]	03:31:52.82	−27:39:31.5	2.3429(1)	965 ± 16	36.0 ± 3.6	47.0 ± 4.2	42.0 ± 4.8	1.9 ± 1.5	4.8	1
SMM J0217−0505	02:17:38.92	−05:05:23.7	2.5305(2)	41 ± 11	24.8 ± 3.6	26.2 ± 4.2	26.0 ± 4.8	7.1 ± 1.5	4.8	2
SMM J0333−2745	03:33:15.43	−27:45:24.4	2.6937(2)	75.8 ± 6.9	31.2 ± 3.6	41.0 ± 4.2	35.3 ± 4.8	9.2 ± 1.2	4.8	3
SMM J2218+0021	22:18:04.42	00:21:54.4	2.5171(4)	44 ± 10	–	–	–	9.0 ± 2.3	4.2	4
SMM J0332−2755	03:32:43.20	−27:55:14.5	2.1236(3)	106 ± 9	32.8 ± 3.6	31.6 ± 4.2	21.2 ± 4.8	5.2 ± 1.4	3.6	5
SMM J2217+0017[a]	22:17:42.25	00:17:02.0	2.2777(2)	58 ± 11	–	–	–	–	9.6	6
RG J0332−2732[a]	03:32:56.75	−27:32:06.3	2.3152(3)	160 ± 20	27.5 ± 3.6	27.5 ± 4.2	20.3 ± 4.8	2.4 ± 1.4	2.4	7
SMM J0217−0503[b]	02:17:38.62	−05:03:39.5	2.0280(3)	185 ± 12	36.3 ± 3.6	33.9 ± 4.2	21.7 ± 4.8	4.4 ± 1.7	4.8	2
SMM J0217−0459	02:17:25.12	−04:59:37.4	2.3090(5)	57 ± 10	21.7 ± 3.6	22.2 ± 4.2	17.0 ± 4.8	4.5 ± 1.9	7.2	2

References: (1) Ivison et al. (2010); (2) Ivison et al. (2007); (3) Biggs et al. (2011); (4) Chapman et al. (2005); (5) Dunlop et al. (2010); (6) Chapman et al. (2004a); (7) Miller et al. (2008).
[a]AGN candidate; [b]broad-line AGN, as discussed in Section 3.3.

cold dark matter (ΛCDM) cosmology with $\Omega_\Lambda = 0.7$ and $H_0 = 71\,km\,s^{-1}Mpc^{-1}$ in which 0.5 arcsec corresponds to a physical scale of ∼4 kpc at $z = 2$ (the median seeing and redshift of our observations and targets, respectively).

2 SAMPLE SELECTION AND OBSERVATIONS

2.1 Sample

Our IFU survey comprises nine radio-identified ULIRGs (listed in Table 1), targeted from various surveys, preferentially chosen from our equatorial and southern fields to enable further study with Atacama Large Millimetre/submillimetre Array (ALMA). *Herschel*-SPIRE fluxes are available for the majority of the sources (Table 1), enabling the far-infrared luminosities of the samples to be derived directly. We find that all sources have $L_{FIR} > 10^{12}\,L_\odot$. The targets designated 'SMM' are SMGs with $S_{850\,\mu m} > 4$ mJy, while those listed as 'RG' are undetected at 850 μm, with typical 3σ rms of 4.5 mJy. These sources are, however, still found to be bright at 250, 350 and 500 μm and therefore represent the ULIRGs with hotter dust temperatures causing the 850-μm fluxes to fall below the detection limits. Eight of the sources have spectroscopic redshifts derived from our long-slit detections of the Hα emission line. For the ninth source, SMM J2217+0017, we obtained the redshift directly with our IFU observations. SMM J2217+0017 was identified as a bright SMG ($S_{1100\,\mu m} = 4.9 \pm 0.7$ mJy) in the SA22 field (Tamura et al. 2009) with a VLA counterpart (Chapman et al. 2004a) and an optical through mid-infrared [*Spitzer*-Infrared Array Camera (IRAC)] photometric redshift constrained to $z \sim 2$–2.5.

The SMGs span a redshift range of $2.0 < z < 2.7$, which covers the median of the parent sample from Chapman et al. (2005), and places Hα in the *K*-band atmospheric window. Fig. 1 shows the range of 1.4-GHz radio (referenced in Table 1) and Hα luminosities in the target sample compared to the larger sample of SMGs studied in Swinbank et al. (2004) and Chapman et al. (2005), demonstrating our IFU sample is representative. We use the radio luminosities and radio-derived SFRs in Fig. 1, rather than the directly measured far-infrared luminosities and SFR_{FIR} values, to enable a comparison to the complete parent sample. Fig. 1 also shows that our sample is consistent with having extinctions of $A_v \sim 2.9$, corresponding to the

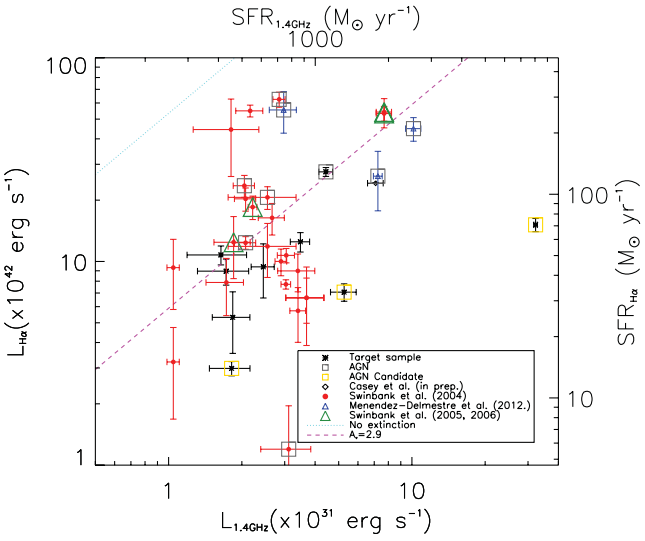

Figure 1. The Hα luminosities from our IFU observations (not corrected for extinction) versus radio luminosities of the sources studied in this work, compared to the sample of SMGs studied in Swinbank et al. (2004) using long-slit spectroscopy. The $SFR_{1.4\,GHz}$ axis represents the SFRs derived from the radio luminosities, using the far-infrared–radio correlation (Ivison et al. 2010) and the conversion to SFR from Kennicutt (1998a). The $SFR_{H\alpha}$ axis assumes the conversion to SFR from Kennicutt (1998a) and both $SFR_{1.4\,GHz}$ and $SFR_{H\alpha}$ conversions include a factor of 1.7 to convert from the Salpeter IMF to Chabrier IMF. The sample of SMGs with previously published IFU observations (Swinbank et al. 2005, 2006; Menendez-Delmestre et al., in preparation) are highlighted. We also plot the Hα luminosity for RG J0332−2758 (Casey et al. 2011) which has IFU observations presented in Casey et al. (in preparation). Our target sample has a similar range of radio and Hα luminosities to the SMGs in Swinbank et al. (2004). The dotted line denotes equality in the two SFR indicators, whereas the dashed line corresponds to the relationship between the two SFR indicators for an extinction of $A_v = 2.9 \pm 0.5$ (the average value for SMGs from Takata et al. 2006) which decreases the observed $SFR_{H\alpha}$ relative to the radio. We also mark the target sources which potentially host AGN, as discussed in Section 3.3 and the previously published sources which are known to host AGN.

average A_v measured for a sample of SMGs from the Hα/Hβ ratio (Takata et al. 2006), which brings the Hα SFRs in line with those inferred from the far-infrared.

2.2 Observations and reduction

Observations of RG J0331−2739, SMM J0217−0505, SMM J0333−2745, SMM J2218+0021 and SMM J0332−2755 were made with the Gemini-NIFS between 2010 September 24 and 2011 February 28 as part of programme GN/2010B/42. The Gemini-NIFS IFU uses an image slicer to take a 3.0 × 3.0 arcsec^2 field and divides it into 29 slices of width 0.103 arcsec. The dispersed spectra from the slices are reformatted on the detector to provide 2D spectro-imaging, in our case using the *K*-band grism covering a wavelength range 2.00–2.43 μm. The observations were performed using an ABBA configuration in which we chopped by 10 arcsec to blank sky to achieve sky subtraction. Individual exposures were 600 s and each observing block was 2.4 ks, which was repeated between three and four times, resulting in the on-source integration times (which do not include the sky observations) given in Table 1.

SMM J2217+0017, SMM J0217−0503, RG J0332−2732 and SMM J0217−0459 were observed with SINFONI on the VLT between 2011 July 13 and September 23 as part of the programme 087.A-0660(A). All of our observations targeted the redshifted Hα and [N II] λλ6548.1, 6583.0 emission lines in the *K* band. We use the $H + K$ grating on SINFONI which gives a spectral resolution $R = 1500$ covering a range of 1.45–2.45 μm. The field of view is sliced into 32 slices, each of which is imaged on to 64 pixels. We chose the width of the slices to be 0.25 arcsec to provide a 8 × 8 arcsec^2 field (obtaining 32 × 64 spectra of the image with each pixel covering 0.25 × 0.125 arcsec^2). We move the target around four quadrants of the IFU for sky subtraction purposes, however retaining the target in the field of view; therefore, the effective field of view is 4 × 4 arcsec^2 for SMM J2217+0017, RG J0332−2732 and SMM J0217−0459 and 4 × 8 arcsec^2 for SMM J0217−0503 where we use only two quadrants in order to observe the entire extended system. The individual exposure times are 600 s with resulting on-source exposure times (which do not include the sky observations) given in Table 1.

We reduced the NIFS data with the standard Gemini IRAF NIFS pipeline and the SINFONI data with the SINFONI ESOREX pipelines, both of which include extraction, sky subtraction, wavelength calibration and flat-fielding. To accurately align and mosaic the individual data cubes, we created white light (wavelength collapsed) images around the redshifted Hα emission line from each observing block and centroid the galaxy within the data cube. These were then spatially aligned and co-added using an average with a 3σ clipping threshold to remove remaining cosmetic defects and cosmic rays. Flux calibration was carried out by observing bright A0V standard stars at similar airmass to the target galaxy immediately after each observing block for both the NIFS and SINFONI observations, and we then also compare the integrated fluxes to those measured from long-slit observations of the targets. From the reduced standard star cubes, we measure a seeing of full width at half-maximum (FWHM) ∼ 0.5 arcsec for both the NIFS and SINFONI observations which corresponds to ∼4 kpc at $z \sim 2$. The spectral resolution of the data (measured from the skylines at ∼2.2 μm) is $\sigma = 1.8$ Å or 25 km s^{-1} for the NIFS observations and $\sigma = 6.3$ Å or 88 km s^{-1} for the SINFONI observations. In all the following sections, quoted line widths are corrected to take account of the instrumental resolution, $\sigma_{\rm corr} = \sqrt{(\sigma^2_{\rm obs} - \sigma^2_{\rm sky})}$.

3 ANALYSIS

3.1 Spatially integrated spectra

In Fig. 2 we show the integrated 1D spectra of the targets with strong Hα detections from our IFU observations. We do not include the weak Hα detection in SMM J0217−0459 since the IFU observations are of low signal-to-noise ratio (S/N) and do not provide further information than the previous long-slit observations. We use the integrated spectra to measure basic properties of the sample (z, $S_{\rm H\alpha}$ and $\sigma_{\rm H\alpha}$) detailed in Table 2. We fit Gaussian profiles to the Hα and [N II] emission lines simultaneously in the integrated spectra. We also attempt to fit a broad Hα component; however, we find in all cases that there is no improvement to the χ^2 of this fit compared to the fit without the broad component, so we do not use the broad component fit. Errors on these values were calculated by altering the fit, changing one parameter at a time and allowing the other parameters to minimize, until the χ^2 changed by 1. We only use the flux from the pixels in which Hα is detected at $>3\sigma$ to create the integrated spectra. For the faint SMM J0217−0459 we quote the Hα redshift (which confirms the redshift gained from previous Hα slit observations), Hα flux and σ, but we are unable to measure any resolved properties. For SMM J0217−0503b we fit a double Gaussian to the Hα profile since it shows a double-peaked disc-like profile. Indeed, the disc-like profile of SMM J0217−0503b is confirmed in Section 4.2.

We measure an average Hα flux of $\langle S_{\rm H\alpha} \rangle = 3 \pm 1 \times 10^{-16}$ erg s^{-1} cm^{-2} and an average velocity dispersion of $\langle \sigma \rangle = 220 \pm 80$ km s^{-1}. In all sources we clearly detect [N II] λ6583 emission except SMM J0332−2755 for which we quote a 3σ upper limit to the ratio of [N II]/Hα. For our total sample, we measure an average [N II]/Hα ratio of 0.52 ± 0.07 in the sources where [N II] was detected. The large spectral coverage of SINFONI allows for measurements of Hβ in the three SINFONI sources. Hβ, however, lies in a noise-dominated part of the spectra such that no useful limit can be placed on the ratio of Hα/Hβ. We therefore use an extinction value of $A_v = 2.9 \pm 0.5$, taken as the average extinction given in Takata et al. (2006), to correct the Hα luminosities since these are dusty systems. The corrected luminosities were converted to SFRs using the conversion from Kennicutt (1998b) which includes a conversion factor of 1.7 to adjust from a Salpeter initial mass function (IMF; Salpeter 1955) to a Chabrier IMF (Chabrier 2003). We apply the extinction correction as detailed in Förster-Schreiber et al. (2009), using the correction at the wavelength of Hα of $A_{\rm H\alpha} = 0.82A_v$. The total correction applied is therefore $10^{0.33A_v}$. We provide the uncorrected Hα fluxes in Table 2 along with the corrected SFRs.

Since we do not have individual extinction estimates to the Hα line, we derive far-infrared luminosities of our SMGs in order to provide unextinct estimates of the SFR. For seven of our SMGs we can use the *Herschel*-SPIRE observations from Data Release 1 (DR1) (Griffin et al. 2010; Oliver et al. 2012) to derive the far-infrared luminosities. We extract the SPIRE fluxes at the positions of our SMGs (Table 1) and fit modified blackbodies to the photometry at the known redshift. In this analysis, we fix the dust emissivity, $\beta = 2$ (Magnelli et al. 2012), but allow the dust temperature and bolometric luminosity to vary. For SMM J2218+0021 and SMM J2217+0017, which do not have 250-, 350- and 500-μm fluxes, we scale the far-infrared SED of SMM J2135−0102 (the well-studied lensed SMG at $z = 2.3$; Swinbank et al. 2010b; Ivison et al. 2011) to the 850-μm flux for SMM J2218+0021 and the 1.1-mm flux for SMM J2217+0017 ($S_{1.1\,\rm mm} = 4.9 \pm 0.7$ mJy). We compare the

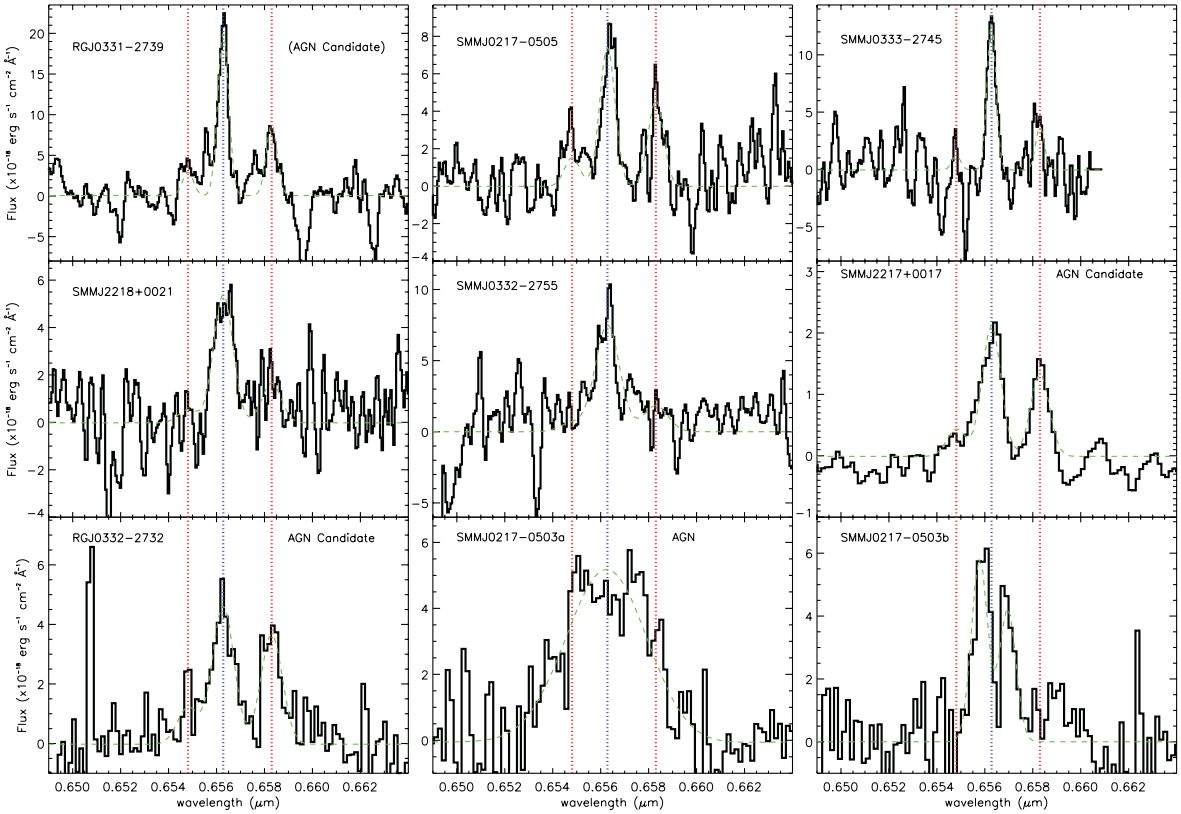

Figure 2. 1D integrated spectra of sources showing the location of the Hα line at 6562.8 μm (blue dotted line) and the [N II] lines at 6583.0 and 6548.1 μm (red dotted lines). The NIFS spectra have been smoothed by 2.3 pixels to match the resolution of the SINFONI spectra. All spectra are continuum subtracted. The dashed lines represent the fit to the Hα and [N II] lines. The large ratios of [N II]/Hα in SMM J2217+0017 and RG J0332−2732 lead us to suggest that these sources may host AGN. We mark RG J0331−2739 as an 'AGN candidate' due to its high radio luminosity; however, the low value of [N II]/Hα and further analysis of the Hα velocity field suggest that the Hα properties are not being driven by the AGN activity. SMM J0217−0503 is divided into its two clear components (as can be seen in the maps of Hα). SMM J0217−0503a is most likely an AGN with broad Hα emission blending with the [N II] lines. SMM J0217−0503b has a disc-like, double-peaked Hα profile.

Table 2. Table of the SMG properties measured and derived from the integrated spectra and maps. The $SFR_{H\alpha}$ values are calculated using Kennicutt (1998a) and include a conversion factor of 1.7 to adjust to a Chabrier IMF. The $SFR_{H\alpha}$ values are extinction corrected using an average extinction of dusty, star-forming ULIRGs of $A_v = 2.9 \pm 0.5$ (Takata et al. 2006). The $SFR_{1.4\,GHz}$ values are calculated from the radio fluxes using the far-infrared–radio correlation (Ivison et al. 2010). The SFR_{FIR} values are calculated from the SED-derived far-infrared luminosities. V_{obs} is the difference between the minimum and maximum velocities measured across the Hα velocity field (taken as the 5th and 95th percentiles of the velocity distribution). We quote the properties of the whole SMM J0217−0503 system as well as the two clear components. The properties of SMM J0217−0503b assume a double Gaussian fit to the disc-like Hα emission-line profile. The broad-line fit to Hα of SMM J0217−0503 and SMM J0217−0503a (the AGN component) covers Hα and the blended [N II] doublet; therefore, it is not possible to measure the [N II] flux. Caution should be taken with the $SFR_{1.4\,GHz}$ value for RG J0331−2739 since the high radio luminosity suggests the radio flux is dominated by the AGN and therefore gives an unphysically high SFR using the far-infrared–radio correlation. The ratios of [N II]/Hα we quote include the flux from the 6583-μm [N II] line only since only this line is included when classing systems as being potentially AGN dominated using the comparison to the data in Kewley et al. (2006).

Source	$S_{H\alpha}$ (10^{-16} erg s^{-1} cm^{-2})	$\sigma_{H\alpha}$ (km s^{-1})	$SFR_{H\alpha}$ ($M_\odot$ yr^{-1})	$SFR_{1.4\,GHz}$ ($M_\odot$ yr^{-1})	SFR_{FIR}	[N II]/Hα (km s^{-1})	V_{obs}	$r_{1/2}$ (kpc)	K_{asym}
RG J0331−2739[a]	3.7 ± 0.3	83 ± 8	600 ± 200	8000 ± 100	280 ± 60	0.41 ± 0.08	120 ± 20	2.99 ± 0.04	0.60 ± 0.05
SMM J0217−0505	2.1 ± 0.2	130 ± 20	500 ± 200	400 ± 100	210 ± 50	0.6 ± 0.1	400 ± 50	2.61 ± 0.05	0.551 ± 0.007
SMM J0333−2745	2.1 ± 0.2	70 ± 10	500 ± 200	870 ± 80	340 ± 50	0.3 ± 0.1	150 ± 30	2.05 ± 0.06	5.5 ± 0.3
SMM J2218+0021	1.8 ± 0.3	170 ± 30	400 ± 200	400 ± 100	500 ± 100	0.2 ± 0.1	380 ± 50	2.88 ± 0.06	1.7 ± 0.1
SMM J0332−2755	2.8 ± 0.8	200 ± 100	400 ± 200	610 ± 60	190 ± 50	<0.7	360 ± 40	2.48 ± 0.1	11 ± 1
SMM J2217+0017[a]	0.75 ± 0.06	150 ± 10	130 ± 50	450 ± 90	900 ± 100	0.7 ± 0.1	300 ± 100	4.8 ± 0.6	0.61 ± 0.05
RG J0332−2732[a]	1.7 ± 0.2	180 ± 20	300 ± 100	1300 ± 200	200 ± 40	0.8 ± 0.1	200 ± 100	3.1 ± 0.3	1.3 ± 0.2
SMM J0217−0503	9.2 ± 0.5	740 ± 40	1200 ± 400	1110 ± 70	190 ± 50	–	800 ± 100	9.0 ± 0.3	3.9 ± 0.3
SMM J0217−0503a[b]	6.4 ± 0.3	740 ± 40	800 ± 300	–	–	–	300 ± 100	4.2 ± 0.3	–
SMM J0217−0503b	1.0 ± 0.1	90 ± 20	120 ± 50	–	–	0.4 ± 0.1	600 ± 100	4.6 ± 0.3	0.249 ± 0.005
SMM J0217−0459	1.3 ± 0.4	100 ± 100	200 ± 100	460 ± 80	150 ± 50	0.4 ± 0.3	–	–	–

[a]AGN candidate;[b]AGN as discussed in Section 3.3.

radio luminosities to the far-infrared luminosities to probe the far-infrared radio correlation. We derive q using equation (1) (Helou, Soifer & Rowan-Robinson 1985):

$$q = \log\left(\frac{L_{\rm FIR}}{9.8\times10^{-15}\,{\rm L}_{\odot}}\right) - \log\left(\frac{L_{1.4\,{\rm GHz}}}{{\rm W\,Hz^{-1}}}\right). \quad (1)$$

We find a median q of 2.0 ± 0.2 for the sources without AGN signatures and a similar $q = 1.9 \pm 0.5$ for our entire sample, which are consistent with the q value of a sample of SMGs studied in Kovács et al. (2006): ($q \sim 2.1$). We convert the derived far-infrared luminosities from the SED fits to SFRs using equation (2), which is the relation from Kennicutt (1998a) adjusted from a Salpeter IM to a Chabrier IMF using a factor of 1.7 :

$${\rm SFR(M_{\odot}\,yr^{-1})} = L_{\rm FIR}({\rm erg\,s^{-1}}) \times 2.6\times10^{-44}. \quad (2)$$

The $\rm SFR_{FIR}$ values are, on average, approximately in line with the extinction-corrected $\rm SFR_{H\alpha}$ values, indicating that using $A_{\rm v} = 2.9 \pm 0.5$ brings the two SFR indicators into agreement.

3.2 Spatially resolved spectra

We use the spatially resolved Hα emission-line maps from our NIFS and SINFONI IFU observations to estimate the distribution of star formation and dynamics within the galaxies. After constructing the data cubes, we proceed to fit the Hα emission line in each pixel. The spectra were averaged over 3×3 spatial pixels (0.15×0.15 arcsec^2 for the NIFS data and 0.375×0.375 arcsec^2 for SINFONI), increasing this up to 5×5 pixels (0.25×0.25 arcsec^2 for the NIFS data and 0.625×0.625 arcsec^2 for SINFONI) if the signal was too low to give a sufficiently high S/N. In regions where this averaging process still failed to give an adequate S/N, no fit was made. Using a continuum fit, we required a minimum S/N of 3 to detect the lines, and when this criterion is met, we fit the Hα emission line with a Gaussian profile, allowing the normalization, central wavelength and width to vary.

We simultaneously fit a double Gaussian to the [N II] lines with the fit to Hα. If the improvement in the χ^2 of this fit, compared to the single Gaussian fit to Hα, is such that $\Delta\chi^2 > 9$ (corresponding to 3σ), then the Hα + [N II] doublet fit is used instead. To calculate the error in the line parameters, we alter the fit parameters one at a time and allowing the other parameters to minimize until $\Delta\chi^2 = 1$, corresponding to a formal 1σ error. Figs 3 and 4 show the results from the line fitting: 2D maps showing the Hα intensity, velocity and velocity dispersion fields. The yellow circles represent the FWHM of the standard stars showing an estimate of the seeing-dominated point spread function (PSF). This estimate is from shorter exposures ($\sim$10 s) than the science exposures and therefore underestimates a possible PSF broadening in the long-exposure science observations. We use the Hα intensity maps to measure the half-light radii, $r_{1/2}$, by summing the Hα flux within increasing circular apertures, centred on the middle pixel of the Hα intensity distribution, until the flux enclosed is equal to half the total flux. The $r_{1/2}$ values are then corrected for the PSF.

Figs 3 and 4 show that in all sources the Hα distribution is extended on scales >5 kpc with an average Hα half-light radius of $\langle r_{1/2}\rangle = 3.7 \pm 0.8$ kpc. We compare our Hα $r_{1/2}$ measurements to molecular gas sizes in SMGs. Tacconi et al. (2006) find a median $r_{1/2}$ of $<2 \pm 0.8$ kpc[1] in their sample of SMGs observed in CO, which is in agreement with additional CO measurements from Engel et al. (2010) (median equivalent radius of 2.2 ± 1.4 kpc) despite the fact that these measurements cover a range of high-J CO transitions possibly tracing different distributions of the gas. These CO sizes are also comparable to the 1.4-GHz radio sizes for SMGs found by Chapman et al. (2004b) and Biggs & Ivison (2008) (median equivalent radius of 1.6 ± 0.4 kpc). These compact sizes are lower than the average half-light radius we measure in the Hα sample (3.7 ± 0.8 kpc), suggesting that the Hα observations trace more of the gas distribution in the SMGs. However, we do not have CO line data and Hα observations in the same sample of SMGs; therefore, comparing the two samples can only be done statistically.

All sources, except SMM J2217+0017 and RG J0332−2732, exhibit multiple peaks in the Hα intensity distributions, with two sources showing clear separations between multiple components (SMM J0332−2755 and SMM J0217−0503). The velocity and velocity dispersion fields are not smooth and do not show evidence for disc-like profiles, which is further addressed in Section 4.2.

3.3 AGN identification

Previous IFU studies of SMGs have mainly targeted galaxies showing strong AGN in their Hα spectra (Swinbank et al. 2005, 2006; Menendez-Delmestre et al., in preparation), whereas the majority of our sample does not display clear Hα AGN signatures. Indeed, the submm and/or far-infrared detections of all the sources in our sample provide a baseline of evidence that they are dominated by star formation (implied $\sim$1000 $\rm M_{\odot}\,yr^{-1}$). In SMGs, AGN are found to only contribute at low levels (<20 per cent) to the bolometric output (Alexander 2004). However, even if an AGN is not dominating the bolometric output, it may still affect the Hα distribution and dynamics, it being energetic enough to drive ionized gas over scales of a few kpc (Nesvadba et al. 2008; Harrison et al. 2012).

Two of our sources (RG J0332−2732 and SMM J2217+0017) have high ratios of [N II]/Hα in their integrated spectra (Fig. 2), indicating that these sources may host an AGN [a limit of [N II]/Hα > 0.7 is typically adopted for AGN-dominated systems (Kewley et al. 2006)]. Given the high SFRs, it is also possible that the high ratios are caused by shock ionization from a galactic wind, as opposed to an AGN ionization field, raising the observed value of [N II]/Hα (van Dokkum et al. 2005). The detection of Hα extended over large scales ($\sim$10 kpc), with no obvious outflow kinematics, further suggests these systems may still be star formation dominated in their Hα kinematics.

We expect the high [N II]/Hα ratio from AGN excitation would typically be concentrated to the inner few kpc. We search the off-nuclear regions of RG J0332−2732 and SMM J2217+0017 for gradients in the [N II]/Hα excitation, finding that SMM J2217+0017 shows very concentrated [N II] ([N II]/Hα = 0.7 ± 0.1), with low [N II]/Hα ([N II]/Hα = 0.3 ± 0.1) in regions around the nucleus, likely indicating a compact AGN core surrounded by star formation.

RG J0332−2732, by contrast, shows continued strong [N II]/Hα outside the central nucleus and observations of the [O III], Hβ emission indicate photoionization by an AGN also (Harrison et al. 2012). The ratio of [N II]/Hα is higher in the northern region of this source ([N II]/Hα = 0.9 ± 0.1 rather than [N II]/Hα = 0.7 ± 0.1 in the southern region). It is therefore possible that the AGN may be ionizing the gas to the north only and the remaining extended Hα dynamics we observe are unaffected by AGN activity. The [N II] velocity field follows the same galaxy-wide rotation pattern as the Hα. However, since there is evidence for the velocity fields in RG J0332−2732 and SMM J2217+0017 to represent gas which is photoionized by

[1] All given measurements of FWHM and linear diameter are converted to equivalent half-light radius by dividing the diameters by 2.

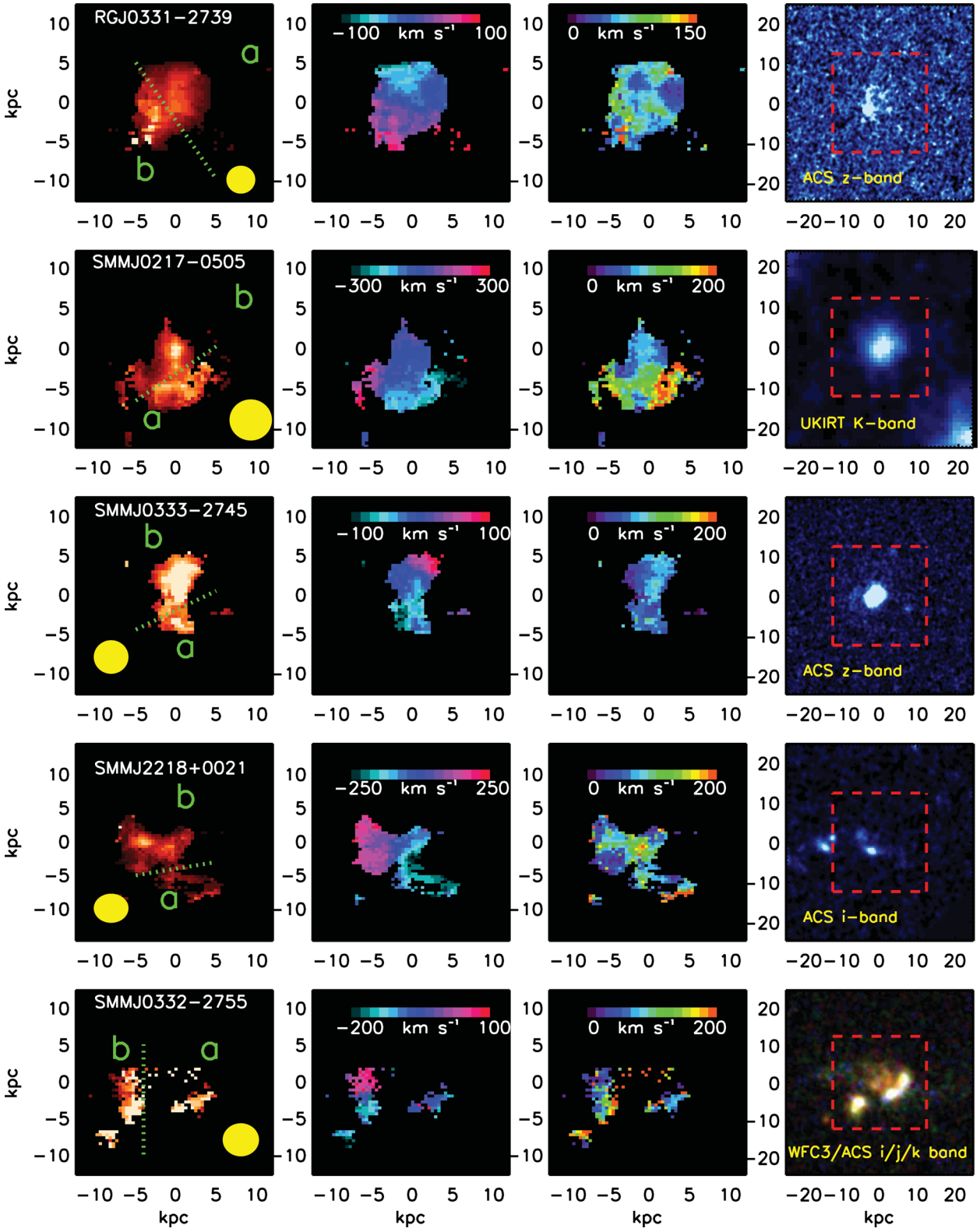

Figure 3. Maps of the properties of the Hα emission lines for each of the five sources observed with NIFS. Left to right: the Hα intensity, Hα velocity and Hα velocity dispersion maps, and the available imaging (we show *HST* imaging if it is available, otherwise we display the ground-based *K*-band imaging). For SMM J0332−2755, imaging in the *i*, *j* and *K* bands are available; therefore, a three-colour image is displayed. The boxes marked by the red dashed lines represent the field of view of NIFS on the imaging. Top to bottom: RG J0331−2739, SMM J0217−0505, SMM J0333−2745, SMM J2218+0021 and SMM J0332−2755. The green dotted lines mark the division into components, labelled as 'a' and 'b'. The yellow circles indicate the FWHM of the seeing-dominated PSF from observations of the standard stars. This estimate from the standard stars is, however, likely better than what is achieved during the long science exposures.

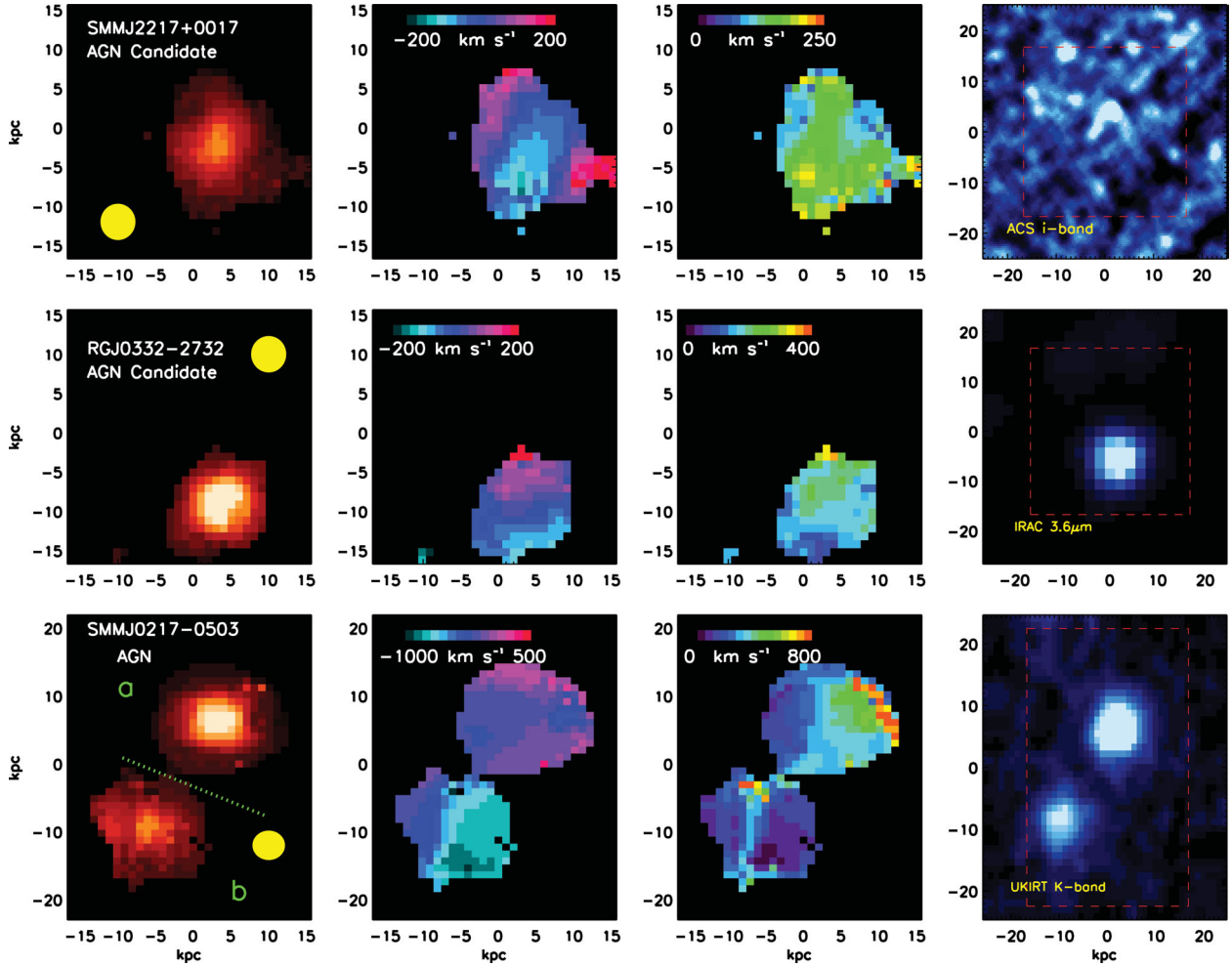

Figure 4. Maps of the properties of the Hα emission lines for each of the three sources observed with SINFONI with strong Hα detections. Left to right: the Hα intensity, Hα velocity and Hα velocity dispersion maps, and the available imaging (we show *HST* imaging if it is available, otherwise we display the ground-based *K*-band imaging or the IRAC 3.6-μm channel map.). The boxes marked by the red dashed lines represent the field of view of SINFONI on the imaging. Top to bottom: SMM J2217+0017, RG J0332−2732 and SMM J0217−0503. The green dotted line marks the division into components for SMM J0217−0503. The yellow circles indicate the FWHM of the seeing-dominated PSF from observations of the standard stars. This estimate from the standard stars is, however, likely better than what is achieved during the long science exposures.

an AGN, given the high [N II]/Hα values, we mark these sources as 'AGN candidates' in the analysis.

The high radio flux of RG J0331−2739 ($S_{1.4\,\mathrm{GHz}} = 965 \pm 16$ μJy) suggests the presence of an AGN. Although it is luminous in the far-infrared as well, the radio luminosity exceeds that expected from the far-infrared–radio relation (Ivison et al. 2010) by a factor of 29. We do not see evidence for any AGN in the Hα, [N II] fields, and the AGN radio core could be very extinct, buried in the system. It is clear from the velocity fields of RG J0331−2739 (Fig. 3 and Section 4.2) that merger kinematics appear to dominate over any possible AGN-driven properties, and the [N II]/Hα ratio lies comfortably within that expected for a $z \sim 2$ star-forming galaxy (Erb et al. 2006). We therefore do not consider this source as an AGN in the remaining analysis for purposes of analysing its nebular line properties.

SMM J0217−0503 is a particularly complex system. It is clear from Fig. 4 that SMM J0217−0503 consists of two spatially separated merging galaxies, with integrated spectra for the individual components shown in Fig. 2. The northern source (SMM J0217−0503a) reveals a broad Hα line indicating a dominant AGN. The southern source (SMM J0217−0503b) appears to be star formation dominated (low [N II]/Hα) with a disc-like velocity field and a double-peaked Hα line profile in the integrated spectrum (Fig. 2). However, both components in this ∼20 kpc separated major merger appear to be far-infrared luminous (e.g. Alaghband-Zadeh et al., in preparation; Bothwell et al. 2012). Although we measure the properties of these two sources in SMM J0217−0503 separately in the following analyses, we consider the whole system as a major merger. We note, however, that the large velocity offset of the two components ($670 \pm 70\,\mathrm{km\,s^{-1}}$) implies that it is possible that this is a flyby system rather than a merger; however, this is dependent on the orientation, configuration and halo mass.

4 RESULTS

4.1 Dynamical properties

In order to test whether the SMGs are distinct in their basic dynamical properties from other galaxy populations, we compare the kinematics of our SMGs to other high-redshift star-forming galaxies studied in previous surveys. In particular, we calculate the ratio

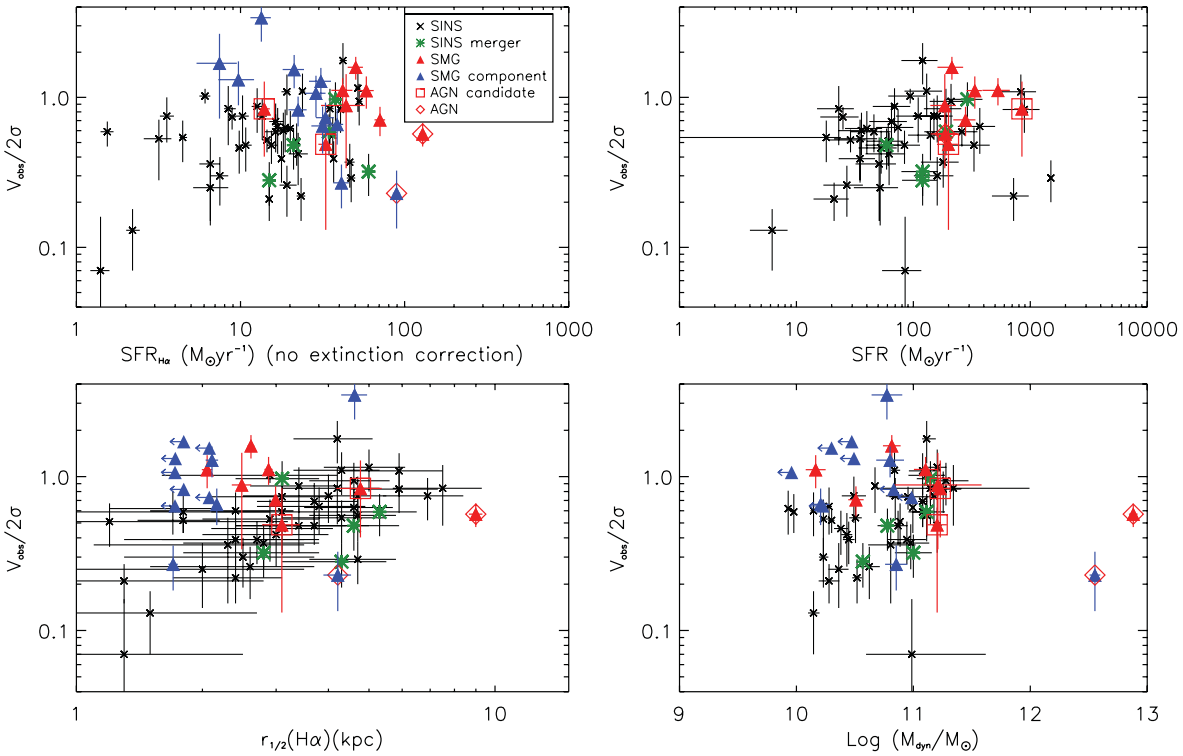

Figure 5. Properties of the SMG sample compared to the sample of SINS galaxies. $V_{obs}/2\sigma$ is ratio of half the observed velocity gradient to the integrated velocity dispersion and provides a measure of how rotation or dispersion dominated a system is. We note that in the case of merging systems $V_{obs}/2\sigma$ is not a direct probe of the physical state of the galaxy since it does not represent the velocity gradient across a single galaxy; however, it remains useful for the comparison of the kinematic fields to the SINS sample. The error bars represent the 1σ uncertainties. Top left: relation between the uncorrected Hα SFRs and $V_{obs}/2\sigma$. Top right: relation between the extinction-corrected Hα SFRs for the SINS sample, the far-infrared SFRs for the SMGs and $V_{obs}/2\sigma$. Bottom left: relation between the Hα half-light radii and $V_{obs}/2\sigma$. Bottom right: relation between the dynamical mass and $V_{obs}/2\sigma$. The masses of the SMG sample represent a useful parametrization in terms of the integrated-velocity dispersion and $r_{1/2}$ for comparison to the SINS sample, but only have a physical representation as a dynamical mass for certain model configurations in virialized systems. We divide SMM J0217−0503 into its two components and mark the northern SMM J0217−0503 source (SMM J0217−0503a) as an 'AGN' (open red diamond) and the southern disc-like component as an SMG. We plot the properties of the whole SMM J0217−0503 system, also marked as an 'AGN'. We highlight RG J0332−2732 and SMM J0332−2732 as 'candidate AGN' (open red squares) since there is some evidence that the velocity fields may be partially affected by AGN given their high values of [N II]/Hα (Section 3.3).

of the maximum velocity across the source to average velocity dispersion, which provides an indicator of the extent to which a system is rotation or dispersion dominated, $V_{obs}/2\sigma$. Here, V_{obs} is the difference between the maximum and minimum velocities derived across the spatial extent of the galaxies, taken as the 5th and 95th percentiles in the velocity distributions determined from the Hα line fitting, while σ is the integrated galaxy velocity dispersion measure derived from the integrated spectra. In Fig. 5, we compare our results to the star-forming galaxies from Förster-Schreiber et al. (2009), UV/optically selected galaxies in a similar redshift range to our sample of SMGs (the SINS sample). The SINS sample contains a wide variety of sources and hereafter comparing to this SINS sample refers to the core majority of the SINS sample of turbulent disc-like systems. We note that the integrated velocity dispersions will be larger than the average dispersions measured in the maps (Figs 3 and 4) since the integrated values contain a non-negligible contribution from the range of velocities within the sources. We compare the average velocity dispersion in the maps to the integrated value finding that, on average, the integrated values are ∼20 per cent larger than the average in the dispersion maps. However, since Förster-Schreiber et al. (2009) use the integrated velocity dispersion in their calculation of $V_{obs}/2\sigma$, we also use the integrated value to enable a consistent comparison.

Fig. 5 shows $V_{obs}/2\sigma$ plotted against the SFRs, Hα half-light radii and the dynamical masses. The average $V_{obs}/2\sigma$ of the SMGs is 0.9 ± 0.1, which is higher than the average of the SINS sample: $\langle V_{obs}/2\sigma \rangle = 0.60 \pm 0.05$. However, the high values of $V_{obs}/2\sigma$ are due to large velocity gradients within the systems rather than especially low velocity dispersions. The average V_{obs} of our SMGs is $330 \pm 80\,km\,s^{-1}$ compared to $160 \pm 20\,km\,s^{-1}$ for the SINS sample, whereas the average integrated velocity dispersion of the SMGs (excluding the AGN SMM J0217−0503) is $130 \pm 20\,km\,s^{-1}$, which is consistent with the average for the SINS sample of $130 \pm 7\,km\,s^{-1}$. The large velocity gradients in the SMGs may be due to the minimum and maximum velocities coming from different components of a merger system. Indeed, the systems which do not have clear subcomponents in Fig. 4 (SMM J2217+0017 and RG J0332−2732) have the lowest values of $V_{obs}/2\sigma$, along with the broad-line AGN component SMM J0217−0503a. The largest value of V_{obs} is in the southern component of SMM J0217−0503b, suggesting a sharp velocity gradient through the disc or possibly a large velocity offset between merging components. When considering merging systems, $V_{obs}/2\sigma$ does not represent the velocity gradient across a single galaxy, and is no longer a direct probe of the physical state of a turbulent disc. However, it remains a useful comparison of the kinematic fields of our SMGs to the SINS

galaxies as we attempt to ascertain how the SMGs differ from typical $z \sim 2$ disc galaxies.

The average $\mathrm{SFR_{H\alpha}}$ of the SMG sample ($41 \pm 7\,\mathrm{M_\odot\,yr^{-1}}$) is somewhat higher than (but within the range of) the SINS sample ($17 \pm 2\,\mathrm{M_\odot\,yr^{-1}}$). Correcting the SMGs for the effects of extinction using $A_\mathrm{v} = 2.9 \pm 0.5$, the average A_v calculated from a sample of SMGs by Takata et al. (2006), raises the SFR values to approximately align with the $\mathrm{SFR_{FIR}}$ values. In the top right-hand plot of Fig. 5 we compare the $\mathrm{SFR_{FIR}}$ values of the SMGs to the extinction-corrected $\mathrm{SFR_{H\alpha}}$ values of the SINS sample since we do not have individual extinction values for the SMGs. We find that the SMGs have higher SFRs, with $\langle \mathrm{SFR_{FIR}} \rangle = 370 \pm 90\,\mathrm{M_\odot\,yr^{-1}}$, than the SINS sample which has $\langle \mathrm{SFR_{H\alpha}} \rangle = 165 \pm 35\,\mathrm{M_\odot\,yr^{-1}}$. The value of A_v used in the SINS sample correction comes from SED fitting and also takes into account the fact that Balmer emission is more attenuated than starlight without a direct measurement of this extra attenuation; therefore, there are significant uncertainties in this correction factor.

The Hα half-light radius measurements for the SMGs span a narrower range than the SINS galaxies, with $\langle r_{1/2} \rangle = 3.7 \pm 0.8$ kpc. The SINS sample have increasing $V_\mathrm{obs}/2\sigma$, with $r_{1/2}$ suggesting that as the size of the galaxies increases, the galaxies become more rotation dominated. Alternatively, as the sizes increase, the velocity differences also increase perhaps due to the velocities having larger ranges when they span larger systems since they lie in more massive haloes; however, when considering merging systems, the size is defined by the merger state rather than the halo mass. This offers an explanation for why we do not observe the strong relationship between $V_\mathrm{obs}/2\sigma$ and $r_{1/2}$ in the SMG sample, since we interpret these systems to be mergers (Section 4.2).

The SMG Hα morphologies and velocity structures clearly show disturbed and complex dynamics, which motivates using a dynamical mass calculation assuming the systems are not dominated by rotation. We therefore use a virial mass approximation (equation 3), which is the method used to calculate dynamical masses for the dispersion-dominated galaxies of the SINS sample, stated by Förster-Schreiber et al. (2009) as being suitable for a wide range of galaxy mass distributions (Binney & Tremaine 2008):

$$M_\mathrm{dyn} = \frac{6.7\sigma^2 r_{1/2}}{G}. \quad (3)$$

Since we interpret the SMGs as being merger systems (Section 4.2) and the velocity dispersions may be driven by the star formation or AGN (Section 5.2), the virial assumption may not be valid. However, this 'mass' provides a useful comparison between the SMGs and SINS galaxies in terms of the integrated velocity dispersion–$r_{1/2}$ parameter space covered. The masses determined from equation (3) of the SMGs span a range from 1.4×10^{10} to $1.6 \times 10^{11}\,\mathrm{M_\odot}$. This does not include the three AGN candidates, which have systematically larger line widths, since the masses calculated using this method may simply reflect the gas motions close to the AGN. Our non-AGN SMG sample shows a similar range to that found in the SINS galaxies, and thus the average velocity dispersions of the SMGs do not obviously distinguish them as more massive; however, the masses are further investigated in Section 5.1. The interpolated rest-frame H-band luminosities of our SMG sample suggest they have similar stellar masses to the SMGs studied in Hainline et al. (2011) (median $\sim 7 \times 10^{10}\,\mathrm{M_\odot}$). This places the stellar masses of the SMGs in the upper third of the estimated stellar masses of the SINS sample which supports the possibility that these ULIRGs may be formed from SINS-type galaxies merging.

To quantify the difference of the two samples in these quantities, we apply a Kolmogorov–Smirnov test (including only the non-AGN component of SMM J0217−0503). We derive a 40 per cent probability that the SINS and SMG samples are drawn from the same distribution in terms of $r_{1/2}$ and 96 per cent for M_dyn, suggesting that the SMGs are not significantly different to the SINS sample in terms of these properties. The probability that the SMGs' $\mathrm{SFR_{FIR}}$ are drawn from the same distribution as the dust-corrected $\mathrm{SFR_{H\alpha}}$ in the SINS sample is 0.02 per cent, while for $V_\mathrm{obs}/2\sigma$ the probability is 2 per cent, suggesting a difference in these quantities between our SMG sample and SINS galaxies.

We also consider how the galaxies in the SINS sample classified as mergers compare to our SMGs. The SINS merger subsample are classified as mergers using kinemetry, the method we use in Section 4.2. Particularly in $V_\mathrm{obs}/2\sigma$ and SFR, the SMGs are distinct from the SINS merger subsample, which may be indicative of the lower luminosity mergers found in the SINS galaxies.

Despite the large difference in their SFRs, the SINS galaxies and SMGs cannot be clearly differentiated simply from basic measures of their velocity difference, velocity dispersion or half-light radius, and so more complex dynamical modelling is required. The SMGs could still represent a mixture of discs and mergers in the same way the SINS sample does, with SMGs being scaled up and more clumpy versions of local discs as seen in the simulations detailed by Davé et al. (2010). When we consider this further in Section 4.2, where the levels of asymmetry in the velocity and dispersion fields are measured, we find strong evidence that the dynamics of all the SMGs are more consistent with being mergers.

4.2 Evidence for mergers and kinemetry analysis

The intensity maps of Figs 3 and 4 show the distribution of star formation within the sources via the Hα morphologies. Six of the sources exhibit clear multiple peaks in Hα intensity, three of which match multiple peaks in imaging, which could in some cases be a result of structured dust within the sources obscuring regions of star formation resulting in clumpy Hα morphology (Swinbank et al. 2010a). The multiple peaks could also be distinct objects which are in the process of merging. The velocity maps show large ranges in the velocities of the systems (typically $400\,\mathrm{km\,s^{-1}}$ peak to peak) and the dispersion maps show disturbed motion within all the sources, providing initial evidence that most of the SMGs could be merger systems. Indeed, only RG J0332−2732 (an AGN candidate) exhibits a smooth velocity and dispersion field.

To better quantify the dynamics, we attempt to fit the 2D velocity field using simple disc models. We parametrize the 2D velocity field using an arctan function of the form $V(r) = (2/\pi)V_\mathrm{c} \arctan(r/r_\mathrm{t})$, where V_c is the asymptotic circular velocity and r_t is the radius at which the rotation curve turns over (Courteau 1997). The model has six free parameters: disc centre $[x, y]$, peak rotational velocity, V_c, r_t, disc inclination (i) and sky position angle. To find the best fit, we use a genetic algorithm with 10 000 possible random fits in each generation, and calculate the χ^2 of each fit. Each parameter is then adjusted towards the best-fitting parameter and the process is repeated until all the values have converged (and we demand >10 generations have passed before testing for convergence). Unsurprisingly, given the complex dynamics seen in Figs 3 and 4, simple disc models do not provide adequate description of the data, with average differences between the best-fitting model and the data of $40 \pm 10\,\mathrm{km\,s^{-1}}$ and a median reduced χ^2 of 60 ± 30. As a control sample, we also run the same fitting procedure on a sample of discs at high redshift (Swinbank et al., in preparation), finding a median

rms of $27 \pm 7\,\mathrm{km\,s^{-1}}$ and reduced χ^2 values between 5 and 8, which suggests the SMGs are not consistent with being disc-like systems.

In order to provide a more definitive test of whether the kinematics are rotation versus merger dominated, we can use kinemetry, which was originally developed to search for non-circular dynamical features in the stellar dynamics of local ellipticals (Copin et al. 2001), but has been extended to the dynamics of high-z galaxies.

The kinemetry described in Shapiro et al. (2008) uses the method detailed in Krajnović et al. (2006), and has been used to identify the mergers in the SINS sample (Förster-Schreiber et al. 2009). This might allow us to better test whether the dynamics of our SMGs are different from SINS galaxies. The asymmetry is measured by fitting ellipses, varying the position angle and ellipticity, to the velocity and dispersion fields.[2] The ellipses are fitted at increasing radii and the coefficients of the Fourier expansion of each best-fitting ellipse at each radius are recorded. These coefficients are then used to establish the level of asymmetry level. The velocity field asymmetry is measured as the average over all radii of

$$v_{\mathrm{asym}} = \left\langle \frac{k_{\mathrm{avg},v}}{B_{1,v}} \right\rangle_r , \tag{4}$$

where $k_{\mathrm{avg},v} = (k_{2,v} + k_{3,v} + k_{4,v} + k_{5,v})/4$ and $k_{n,v} = \sqrt{A_{n,v}^2 + B_{n,v}^2}$ and where $A_{n,v}$ and $B_{n,v}$ are the coefficients of the Fourier expansion of the best-fitting ellipse. The velocity dispersion field asymmetry is measured as the average over all radii of

$$\sigma_{\mathrm{asym}} = \left\langle \frac{k_{\mathrm{avg},\sigma}}{B_{1,v}} \right\rangle_r , \tag{5}$$

where $k_{\mathrm{avg},\sigma} = (k_{1,\sigma} + k_{2,\sigma} + k_{3,\sigma} + k_{4,\sigma} + k_{5,\sigma})/5$ and $k_{n,\sigma} = \sqrt{A_{n,\sigma}^2 + B_{n,\sigma}^2}$ and where $A_{n,\sigma}$ and $B_{n,\sigma}$ are the coefficients of the Fourier expansion of the best-fitting ellipse.

The two asymmetry measures are combined together as $K_{\mathrm{asym}} = \sqrt{v_{\mathrm{asym}}^2 + \sigma_{\mathrm{asym}}^2}$. Systems with $K_{\mathrm{asym}} > 0.5$ are classified as mergers. This limit is determined by running the kinemetry analysis on template merger and disc systems, detailed in Shapiro et al. (2008), to find the two populations separate at $K_{\mathrm{asym}} \sim 0.5$.

We fit the centres of the ellipses first and then we rerun the kinemetry 100 times per source varying the centres within the standard deviation of the initial centre fit. The v_{asym} and σ_{asym} values we quote in Fig. 6 are the bootstrapped median and standard deviation of these 100 runs. The K_{asym} values we quote (in Table 2) are the bootstrapped median and standard deviation of the 100 runs (rather than using the median v_{asym} and σ_{asym} values). Owing to the lower quality of the velocity and dispersion maps of SMM J0332−2755, we bin the maps by 2×2 pixels in order the run the kinemetry.

In Fig. 6 we compare the levels of asymmetry in the velocity and dispersion fields to a number of observed and simulated systems, detailed in Shapiro et al. (2008). The SMGs have, on average, higher levels of asymmetry than both the low-redshift ULIRG population and the more 'normal' star-forming galaxies of the SINS sample. The SMGs also do not lie close to the SINGS low-redshift spiral galaxies, confirming that the SMGs are very different to other populations of star-forming galaxies in terms of their gas dynamics.

The background red–blue pixels represent the results of running the kinemetry on the template discs and mergers provided by Shapiro et al. (2008). We find all of the systems in our sample of SMGs have $K_{\mathrm{asym}} > 0.5$ (Table 2), and thus we classify all the systems as mergers. We also calculate the level of asymmetry in the southern component of SMM J0217−0503, finding that $K_{\mathrm{asym}} < 0.5$, which suggests that this component is a disc-like source (as implied in Figs 2 and 4), merging with the northern AGN source. Indeed, the K_{asym} value for the entire system is 3.9 ± 0.3, and therefore the whole system is clearly classed as a merger. The sources which are the closest to the disc region of Fig. 6 are the AGN candidate source (SMM J2217+0017), RG J0331−2739 and the disc component of SMM J0217−0503 (the southern component in a major merger). However, the K_{asym} values for SMM J2217+0017 and RG J0331−2739 (using the bootstrapped median of the 100 runs) put these sources in the merger class. Therefore, we classify all systems as mergers.

The velocity and dispersion maps cover, on average, a total area of $\sim 160\,\mathrm{kpc}^2$ (at $z = 2$). The spatial resolution of the observations is 0.5 arcsec corresponding to an area of $\sim 16\,\mathrm{kpc}^2$; therefore, on average we have ~ 10 resolution elements in each map. We perform an identical analysis on our SMGs to that done on the SINS sample, which have similar spatial extent. We note, however, that the fit is formally underconstrained and as such, where we find a disc solution, we cannot completely rule out an underlying merger.

We also plot the asymmetry values determined from running the kinemetry on a sample of simulated SMGs at $z = 2$ from Davé et al. (2010). We find these simulated SMGs have a range of asymmetry values forming a sample of both discs and mergers, and our observations are not in complete agreement with the simulated systems since we do not observe the range of discs predicted by the simulations. We perform a 2D Kolmogorov–Smirnov test on the model SMGs and observed SMGs to find the probability that both samples are drawn from the same distribution of 0.1, and therefore we cannot rule out that the simulated SMGs represent the observed SMGs. Further, the merger-like kinematics in these simulations does not necessarily imply that the high infrared luminosity is being driven by a merger event, since some of these simulated galaxies are not actively merging.

There is therefore considerable evidence for the SMGs to be merging systems: the multiple peaks in the Hα intensity fields, the disturbed velocity and dispersion fields to which 2D disc models could not be fitted, the distinction in some integrated quantities between the SMGs and the SINS star-forming galaxies, and finally the kinemetry analysis which classes the SMGs as mergers.

4.3 Subcomponents and separations in the Hα intensity field

Having established that the Hα dynamics of the SMGs are likely merger driven, we next try to identify the components which are in the process of merging, as we have done already for the obviously distinct SMM J0217−0503a and SMM J0217−0503b. We noted before that some of the systems have clearly separated Hα intensity peaks, and in more than half the sample these clearly align with structured velocity dispersion peaks, as would be expected for merging, self-gravitating components. The sources are therefore split into components by identifying the minima in the intensity maps, placing the two intensity peaks in different components, as shown by the green dotted lines in Figs 3 and 4.

The components of SMM J2218+0021 and SMM J0332−2755 also match the components seen in the *Hubble Space Telescope* (*HST*) imaging shown in Fig. 3. We find the division is possible in all sources except the AGN candidates SMM J2217+0017 and RG J0332−2732. It should be noted that splitting the sources into components does not necessarily represent two distinct objects which are merging since these systems could be in the later stages of merging where multiple passes have mixed the gas and stars. However, we

[2] Employing the code: http://www.eso.org/~dkrajnov/idl/

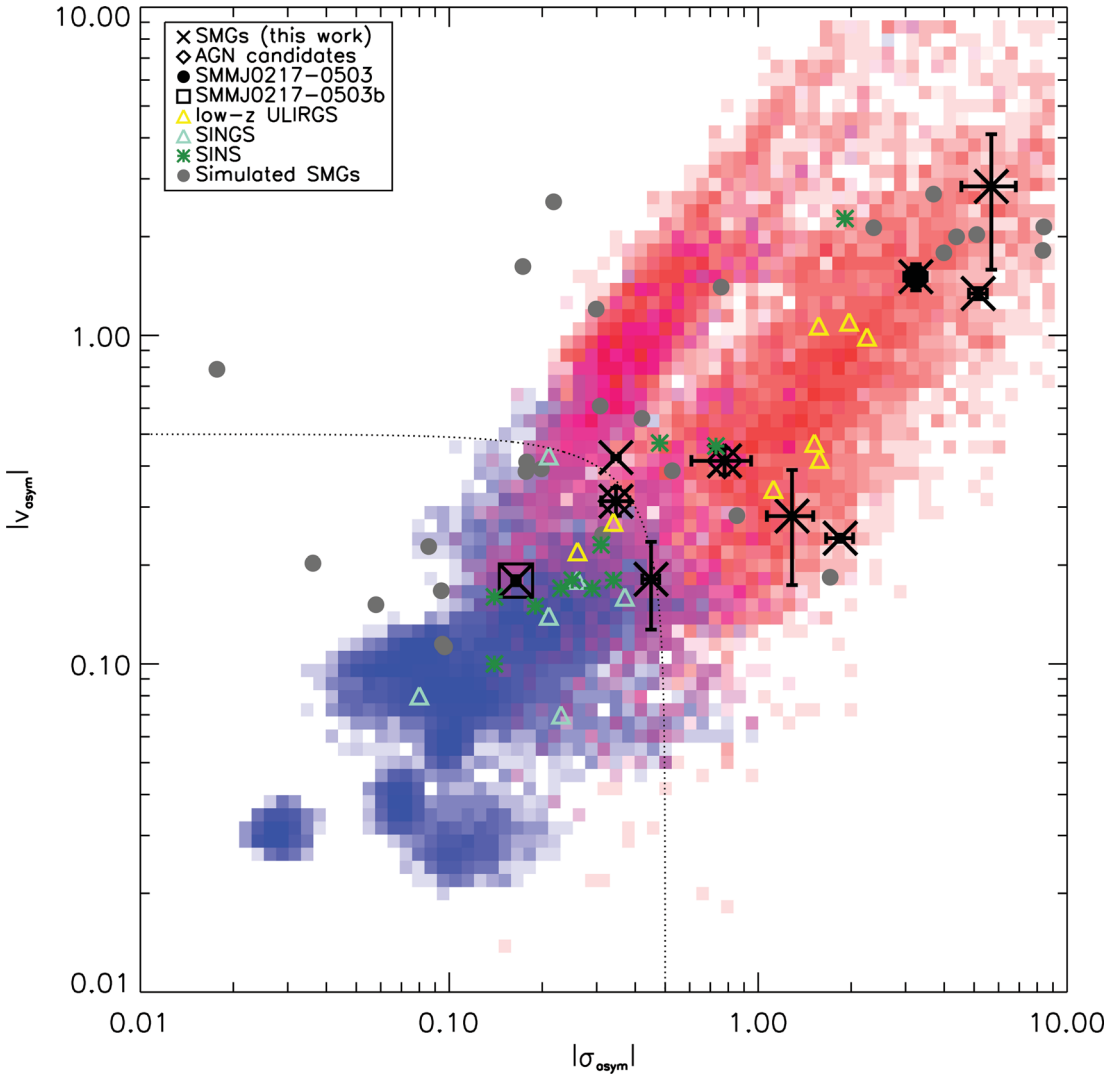

Figure 6. The asymmetry measures of the velocity and velocity dispersion fields for the sample of SMGs compared to a number of other samples; the SINGS sample of local spiral galaxies, a sample of low-redshift ULIRGs, the SINS sample of $z \sim 2$ star-forming galaxies, details of which are given by Shapiro et al. (2008). The background red–blue points are the results of running the analysis on template discs and mergers taken from Shapiro et al. (2008). All of the SMGs lie in the merger region (red background) classifying all of the SMGs as mergers. We highlight the AGN candidates, RG J0332−2732 and SMM J2217+0017 and the whole SMM J0217−0503 system containing the AGN and disc, and we also plot the asymmetry values of SMM J0217−0503b only (disc-like component of the merging system). We plot the results of running the kinemetry on a sample of simulated SMGs at $z = 2$, finding they represent a range of discs and mergers.

discuss the component properties as a reference point assuming that we have identified real merging components, acknowledging that these systems may reflect more complex dynamics than a simple merging pair.

A 2D disc model is well fitted to the southern component of SMM J0217−0503(b) with a reduced χ^2 of 1.4, and higher order moments (kinemetry) also clearly identify this southern component as a coherent disc (detailed in Section 4.2). However, we also note that two regions within SMM J0217−0503b (the eastern and western halves) show different (low) ratios of [N II]/Hα (0.44 ± 0.07 and 0.25 ± 0.07 for the eastern and western sections, respectively). If not dominated by ionization effects, then this suggests that this component may contain regions of varying metallicity and therefore could itself be the product of a recent merger.

We derive $V_{\rm obs}/2\sigma$, $r_{1/2}$, $M_{\rm dyn}$ and $\rm SFR_{H\alpha}$ for the components in the same way as for the whole systems (shown in Fig. 5). The components exhibit similar $V_{\rm obs}/2\sigma$ values to the entire merging systems since $V_{\rm obs}$ and σ are both smaller in the components ($\langle V_{\rm obs}\rangle = 260 \pm 40\,{\rm km\,s^{-1}}$ and $\langle\sigma\rangle = 110 \pm 10\,{\rm km\,s^{-1}}$). The comparison of our SMGs' merging components with SINS galaxies suggests it is possible that the merger of two typical SINS isolated disc galaxies may generate an SMG. However, the properties of the individual components will develop throughout the merger, evolving with each pass, and therefore our division into components may not correctly separate the two progenitor merging sources.

In Fig. 7 we show the spatial offsets for our sample, as well as for a sample of SMGs observed in CO, and previous Hα studies. These are compared to local (Veilleux, Kim & Sanders 2002) ULIRGs which have multiple components with small separations (<4 kpc apart), a few having components up to 25 kpc away. This matches merger simulations (Mihos & Hernquist 1996) where the large burst of star formation occurs at the final stage of the merger, and thus the

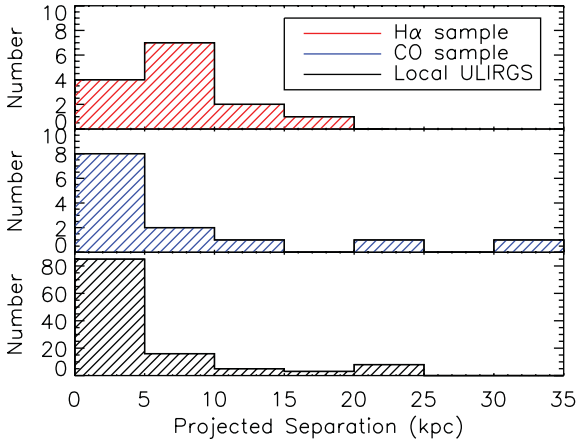

Figure 7. Histograms showing the distributions of the projected separations of the SMGs (Hα observations in the top plot and CO observations in the middle plot) and a sample of local ULIRGs (bottom). The Hα observations combine the NIFS and SINFONI samples with all existing IFU samples detailed in Swinbank et al. (2006) and also including those detailed in Tecza et al. (2004), Swinbank et al. (2005) and Menendez-Delmestre et al. (in preparation). RG J0332−2758 from Casey et al. (in preparation) is also included. The Hα studied SMGs have larger separations on average than local ULIRGs, suggesting different merger stages highlighted by each population. This large separation is not seen in the CO observed SMG sample, potentially highlighting the differences in the gas distributions traced by Hα and CO.

ULIRGS are expected to be observed in very close configurations. This is, however, not observed in the SMGs with most of the Hα sample having separations greater than 4 kpc, indicating that the ULIRG phase can occur at the early stages of merging in these high-redshift systems. The large separations observed in CO are predicted by hydrodynamical simulations (Hayward et al. 2011a) which explains the 850-μm source population.

These three samples are complete with the local ULIRGs being cut at $L_{\rm IR} = 10^{12}\,{\rm L}_{\odot}$ and both the CO and Hα SMG samples spanning a narrow range of $L_{\rm IR} = 2$–$10 \times 10^{12}\,{\rm L}_{\odot}$. There is, however, a selection bias since subcomponents with $r < 4$ kpc would not be resolved in the Hα data. Furthermore, the NIFS Hα sample is not sensitive to separations greater than 15 kpc as the field of view of NIFS is approximately $30 \times 30\,{\rm kpc}^2$ (at $z = 2$), whereas the CO SMG sample could detect separations up to ∼30 kpc. The maximum separation detectable by SINFONI is 30 kpc at $z = 2$ due to the larger total field of view of SINFONI; however we nod the source around four quadrants of the IFU and therefore the effective field of view is approximately $30 \times 30\,{\rm kpc}^2$.

5 DISCUSSION

The multiple Hα peaks, the failed disc fits to the velocity fields and the kinemetry analysis together provide considerable evidence that these systems are likely to be major mergers. We directly identify multiple components in the majority of the systems and suggest that these are in the process of merging. Our findings agree with those of Swinbank et al. (2006) and Menendez-Delmestre et al. (in preparation) who also find multiple-component complex systems in their Hα observations of SMGs. These findings align with the conclusions made by Engel et al. (2010), whose CO observations suggest that SMGs are often formed in mergers, and also with those by Riechers et al. (2011a,b) which detail Extended Very Large Array (EVLA) observations of three SMG systems in CO($J = 1$–0) presented as either early stage or late stage mergers. Next we further explore the multicomponent nature of the SMG systems and study the observed offsets in the context of the parent dark matter haloes.

5.1 Masses from component properties

SMGs have a clustering length $r_0 \sim 8$ Mpc (Blain et al. 2004; Hickox et al. 2012) consistent with a form of evolution, ensuring their properties subsequently match the clustering of $z \sim 1$ evolved red galaxies, and finally of galaxy clusters near the present. This should indicate that they occupy the largest dark matter haloes ($\sim 10^{13}\,{\rm M}_{\odot}$). In order to examine whether the multiple components of the SMGs can be used as a test of the halo mass, we investigate the relationship between the projected separations and the velocity offset of the components.

Fig. 8 shows the spatial and velocity offsets of the components within each of our systems, combined with those from previous SMG Hα-IFU and CO observations summarized in Swinbank et al. (2006), along with two additional SMGs with Hα-IFU measurements in Menendez-Delmestre et al. (in preparation) and Casey et al. (in preparation). We also plot the two SMGs in our sample which cannot be divided into components (the AGN candidates SMM J2217+0017 and RG J0332−2732) with dV and dR limits. The velocity offset for these sources is the difference between the minimum and maximum velocities in the systems ($V_{\rm obs}$) and the spatial offset is $r_{1/2}$, since we assume that if there was a recent merger, it has progressed so that the initial systems are less than $r_{1/2}$ apart and the velocity difference must be below $V_{\rm obs}$.

Fig. 8 highlights that the CO measurements have generally found significantly smaller component separations than this combined sample of IFU Hα maps ($\langle {\rm d}R\rangle = 4 \pm 1$ kpc for the CO sample compared to $\langle {\rm d}R\rangle = 10 \pm 3$ kpc for the complete Hα sample), while the CO velocity offsets extend to high values, with an average of $440 \pm 90\,{\rm km\,s^{-1}}$ compared to $230 \pm 40\,{\rm km\,s^{-1}}$ for the Hα sample, consistent with virialized halo models from Swinbank et al. (2006). These clear differences between the CO and Hα samples may be indicative of the sensitivity of Hα to lower levels of star formation offset from the bright CO region. Indeed, Swinbank et al. (2005) and Menendez-Delmestre et al. (in preparation) have clearly demonstrated this to be the case for these two SMGs with both measurements.

Both the spatial and velocity offsets found from the Hα components in our SMGs are similar to that of the other SMGs observed in Hα with IFUs ($\langle {\rm d}R\rangle = 7 \pm 1$ kpc, $\langle {\rm d}V\rangle = 180 \pm 50\,{\rm km\,s^{-1}}$ and $\langle {\rm d}R\rangle = 8 \pm 2$ kpc, $\langle {\rm d}V\rangle = 200 \pm 100\,{\rm km\,s^{-1}}$ for the literature sample and the sample in this work, respectively). SMM J0217−0503 is an outlier in the plot with its extremely large spatial and velocity offsets. Given the similarities in overall properties of these various SMGs, we cannot attribute this difference to anything other than small sample variance. However, the wider range of dV found in our expanded SMG sample does make a simple virialized halo model, as adopted in Swinbank et al. (2006), a less satisfactory description of this data set.

Our goal is to estimate dynamical halo masses for these galaxies, but this is non-trivial for what then may often be unvirialized systems, and so we turn to N-body simulations and extract the average dR and dV for a set of massive haloes from the Millennium Simulation (Springel et al. 2005b). In Fig. 8 we show the projected spatial and velocity offsets for bound subhaloes within dark matter haloes of total mass (M). All haloes within each mass range are identified and the position and velocity of the most bound subhalo within each is extracted. All the remaining subhaloes are then identified and the

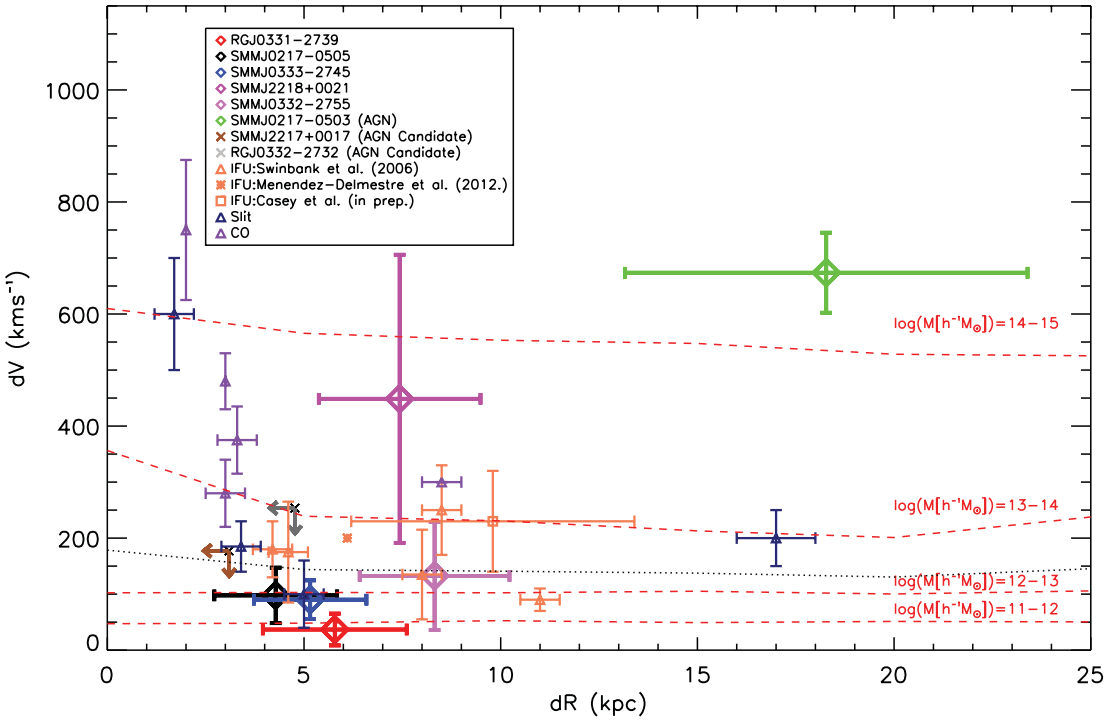

Figure 8. Relationship between the offset in position and velocity of the components within the SMGs. Included are the limits on the separations for the two sources which cannot be divided into components (the AGN candidates SMM J2217+0017 and RG J0332−2732). The outlier is the AGN-disc system of SMM J0217−0503 with a large velocity offset between the two systems. We include the offsets detailed in Swinbank et al. (2006) from their IFU observations, and also their compilation of other IFU offsets and those measured from long-slit and CO observations (Frayer et al. 1998; Genzel et al. 2003; Neri et al. 2003; Kneib et al. 2004; Greve et al. 2005; Tacconi et al. 2006). SMM J123549.44 (Menendez-Delmestre et al., in preparation) and RG J0332−2758 (Casey et al., in preparation) are also plotted. The dashed lines represent the median projected offset between the most bound subhalo and the other subhaloes within dark matter haloes in the quoted mass range from the Millennium Simulation (Springel et al. 2005b). The dotted line represents the interpolation to $\log(M_{\rm halo}[h^{-1}\,{\rm M}_{\odot}]) = 12.8^{+0.3}_{-0.5}$, the SMG halo mass measured from clustering (Hickox et al. 2012). The observed offsets and the measured offsets from the simulation data base are not corrected for viewing orientation of the randomly orientated systems.

spatial (dR) and velocity (dV) offsets between these subhaloes and the most bound subhalo are calculated for each mass range. We then bin the data in bins of dV and plot the median in each bin to create the tracks for each halo mass.

The mass range of $13 < \log(M[h^{-1}\,{\rm M}_{\odot}]) < 14$ appears to best represent the combined data set. For comparison, we show the interpolated relationship to $\log(M_{\rm halo}[h^{-1}\,{\rm M}_{\odot}]) = 12.8^{+0.3}_{-0.5}$, the SMG halo mass measured from clustering (Hickox et al. 2012), which is lower than the average halo mass we derive. However, the bias of SMGs to haloes is potentially quite complicated (Chapman et al. 2009), given the short duration of the burst and the unknown range of environments that they occur in.

The large spatial and velocity offsets of SMM J0217−0503 suggest this system could have a $\log(M[h^{-1}\,{\rm M}_{\odot}]) \sim 14$ halo, which we view along the line-of-sight velocity, or an even larger halo mass if it is not in this preferred viewing orientation, providing evidence that SMGs may sometimes be beacons for massive protoclusters of galaxies ($\log(M[h^{-1}\,{\rm M}_{\odot}]) > 14$) (Chapman et al. 2009; Tamura et al. 2009; Matsuda et al. 2011). In the Millennium Simulation data base there are 28 haloes with masses $14 < \log(M[h^{-1}\,{\rm M}_{\odot}]) < 15$, confirming that these large masses are possible and therefore that the two components of SMM J0217−0503 are likely part of a common halo rather than two separate sources whose projection places them within our field of view. However, we note that it is also possible that the SMM J0217−0503 system may represent a flyby rather than a merger owing to the large velocity offset of $670 \pm 70\,{\rm km\,s^{-1}}$.

5.2 High velocity dispersions and the relationship to SFR density

Figs 3 and 4 clearly show resolved substructure in the Hα velocity dispersion maps which often correlate with the intensity fields. We further investigate this relationship and explore the origin of the high velocity dispersions found in our SMGs. Despite the larger $V_{\rm obs}/2\sigma$ in the SMGs compared to the SINS galaxies, the values are significantly lower than observed in local discs ($v/\sigma \sim 2$–5; Hunter et al. 2005) which have much lower dispersions but comparably large circular velocities. Given our findings (in Section 4.2) that the asymmetrical velocity and dispersion fields enable us to classify the systems as mergers, it is natural that the high velocity dispersions within our sample may be due to the merging systems causing the gas to be disturbed.

The SINS galaxies with high velocity dispersions are explored in Genzel et al. (2008) within the context of disc-like galaxies displaying turbulent motion. They explain the turbulent, rotating disc structures either using feedback from the star formation driven by supernova winds (Efstathiou 2000), or with accreting gas driving the turbulence as it flows into the disc from the dark halo (Genzel et al. 2006). By contrast, the simulations of Davé et al. (2010) suggest turbulent motion in massive disc-like galaxies is driven by harassment by smaller satellites and the infall of gas. In the SMGs, the high Hα velocity dispersions may also be connected to the star formation itself, rather than the forces acting on the gas from the merger.

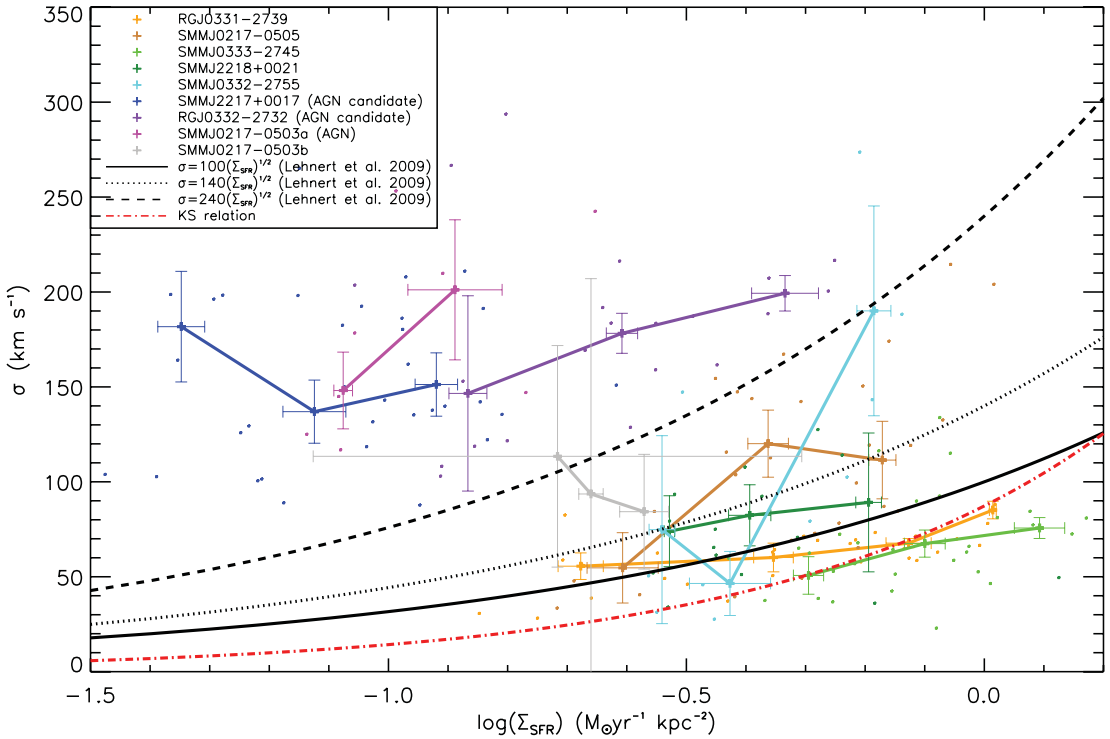

Figure 9. Velocity dispersion against the star formation intensity per pixel for each source. The dot–dashed line represents the relation for the case if the velocity dispersion values are purely a result of the KS relation. The dashed, dotted and solid lines represent models, detailed in Lehnert et al. (2009), describing the relation between the velocity dispersion and the star formation intensity per pixel if the energy from the star formation is powering the motion of the gas. The three lines assume three efficiencies of the coupling between the input energy by stars and the ISM. The sources follow tracks along the plot despite being offset from each other. The SFRs are not extinction corrected. All data cubes are smoothed to match the seeing of 0.6 arcsec and then binned so that each pixel is $0.25 \times 0.25\,\mathrm{arcsec}^2$ except for SMM J0217−0503b. Since we observe the disc-like double-peaked Hα profile in SMM J0217−0503b, we plot the velocity dispersion and star formation intensity in three distinct regions across the source instead of using the results from the line-fitting procedure which blend the double peak as a single line.

We first test whether the relationship between the velocity dispersions and the SFRs can be explained as being purely a result of the Kennicutt–Schmidt (KS) star formation density–gas relation (Kennicutt 1998b):

$$\Sigma_{\mathrm{SFR}} = A\Sigma_{\mathrm{gas}}^{n} \tag{6}$$

we relate Σ_{gas} to the velocity dispersion (σ) by setting Toomre Q criterion to equal to 1, since we assume the gas finds a stable disc configuration in a short time as suggested by hydrodynamical simulations (Springel, Di Matteo & Hernquist 2005a), where

$$Q = \frac{\kappa\sigma_{\mathrm{gas}}}{\pi G\Sigma_{\mathrm{gas}}} \tag{7}$$

and $\kappa = \sqrt{2}V/r$ (Schaye & Aguirre 2005), where we take $V = V_{\mathrm{obs}}$ and $r = r_{1/2}$. We take A to be $10^{-3.63}$ and $n = 1.27$, as derived in Genzel et al. (2010).

We plot this relation in Fig. 9 to enable a comparison to the observed relations between the Hα velocity dispersion per pixel and the star formation intensity. We note first that there are several selection effects at work. There are sections of the σ–Σ_{SFR} plane which cannot be populated from the observations. The upper-left region of Fig. 9 is empty as broad lines with low star formation intensities have too low S/N for Gaussian fitting. There is also a lower limit to the velocity dispersion restricted by the spectral resolution and the lower region ($\lesssim$50 km s^{-1}) cannot be populated.

The high velocity dispersion per pixel values of our three SMGs showing some AGN characteristics could be arising from ionization of gas in the broad- and narrow-line regions of the AGN itself, and it is possible that the lower Hα densities in these sources are due to feedback from the AGN inhibiting the star formation in the regions surrounding the AGN (Nesvadba et al. 2008). One star formation dominated SMG, SMM J0217−0503b, which has intrinsically narrow lines, is not sufficiently resolved spatially to separate the double-peaked rotation profile in the central region, and our line-fitting procedure blends this double peak as a single line. We therefore choose three distinct regions within the source and use the integrated spectra of these regions to obtain the velocity dispersion and SFRs, allowing a fit to the double peak.

Fig. 9 shows that the KS relation does not describe the data well since the majority of the data have higher values of velocity dispersions at a given star formation intensity than predicted by this model. Clearly, both the dust extinction and inclination will have a dramatic effect on the location of these tracks. An average $A_{\mathrm{v}} = 2.4 \pm 0.6$ is required for the SMGs (excluding the AGN candidates) to match this Σ_{SFR}–σ relation, which is compatible with the average implied dust correction derived for SMGs (e.g. Smail et al. 2004; Swinbank et al. 2004; Takata et al. 2006), and suggestive that SMGs simply follow the standard KS law (as suggested may be the case by Ivison et al. 2011).

Since we cannot constrain the dust extinction or inclination angle from our data, we also consider if the velocity dispersions are driven by the star formation itself. We follow the same analysis as carried out in Lehnert et al. (2009) when exploring the source of the turbulence in SINS galaxies. The SMGs are comparable to

the SINS galaxies, with the majority of the data lying within the range spanned by the relations from Lehnert et al. (2009) which represent the plausible ranges in efficiency of the energy transfer from the star formation to the gas. It is therefore possible that it is the star formation which drives the velocity dispersion. However, it is also possible that the turbulence is driven by the merging processes which stir up the gas. We require extinction maps to establish the true star formation intensities in order to further test these hypotheses.

6 CONCLUSIONS

We analyse subarcsecond resolution Hα line data, taken using the integral field spectrometers Gemini-NIFS and VLT-SINFONI, of nine SMGs with $2.0 < z < 2.7$. The gas dynamics and morphologies were mapped by tracing the Hα line within the eight of the sources. We compare the velocity fields in this sample to a sample of UV/optically selected star-forming galaxies at the same redshift (studied in the SINS survey), finding that the SMGs are kinematically distinct, with higher SFRs and larger velocity gradients across the systems. The majority of the SMG sample are not consistent with being disc-like systems with multiple peaks in Hα intensity and irregular and turbulent velocity and velocity dispersion fields. This is confirmed from the kinemetry analysis which classes all systems as mergers rather than discs. We identify multiple components in six of the sources, further confirming the suggestion that most SMG star bursts are triggered in major mergers (Engel et al. 2010).

We bring together all existing IFU Hα observations of SMGs and use the spatial and velocity offsets between the components of the merging systems to infer an average halo mass, $13 < \log(M[h^{-1}\,\mathrm{M}_{\odot}]) < 14$, for the systems which is higher than the mass predicted from clustering measurements.

We observe higher values of $V_{\rm obs}/2\sigma$ in the SMG sample compared to the SINS galaxies due to the large $V_{\rm obs}$ values measured across merging components. The velocity dispersion values in the SMGs are larger than observed in local discs. We explore the origin of this turbulence, finding that the disturbed gas motions are consistent with the KS law and variable extinctions, but might also be driven by the merging torques or even the star formation itself.

Analysing the outputs from the various simulation of SMGs in an identical way to the observations will enable us to better determine which situation best describes the trigger for the ULIRG phases in these galaxies. Initial evidence from the kinemetry analysis of the simulated SMGs suggests that the simulated systems are a mixture of discs and mergers. By better understanding the triggers of the ULIRG phases, we can also probe the build of mass in some of the most massive galaxies in the Universe and investigate if these SMGs are the progenitors of the massive elliptical galaxies observed today (González et al. 2011; Hainline et al. 2011).

ACKNOWLEDGMENTS

This paper is based on observations made with Gemini-North under programme number GN/2010B/42 and ESO Telescopes under programme number 087.A-0660(A). The Gemini Observatory is operated by the Association of Universities for Research in Astronomy, Inc., under a cooperative agreement with the NSF on behalf of the Gemini partnership: the National Science Foundation (United States), the Science and Technology Facilities Council (United Kingdom), the National Research Council (Canada), CONICYT (Chile), the Australian Research Council (Australia), Ministério da Ciência, Tecnologia e Inovação (Brazil) and Ministerio de Ciencia, Tecnología e Innovación Productiva (Argentina). We thank Kristen Shapiro for supplying the kinemetry values for template discs and mergers. SA-Z thanks Paul Hewett for his valuable comments and support. SA-Z, CMH and DMA acknowledge the support from STFC. DN acknowledges support from the US National Science Foundation via grant AST-1009452. AMS acknowledges an STFC Advanced Fellowship. IS acknowledges support from STFC and through a Leverhulme Senior Fellowship. This research has made use of data from HerMES project (http://hermes.sussex.ac.uk/). HerMES is a Herschel Key Programme utilizing Guaranteed Time from the SPIRE instrument team, ESAC scientists and a mission scientist. HerMES will be described in Oliver et al. (2012). The HerMES data were accessed through the HeDaM data base (http://hedam.oamp.fr) operated by CeSAM and hosted by the Laboratoire d'Astrophysique de Marseille.

REFERENCES

Alexander D. M., 2004, in Mújica R., Maiolino R., eds, Multiwavelength AGN Surveys. World Scientific Press, Singapore, p. 129
Baugh C. M., Lacey C. G., Frenk C. S., Granato G. L., Silva L., Bressan A., Benson A. J., Cole S., 2005, MNRAS, 356, 1191
Biggs A. D., Ivison R. J., 2008, MNRAS, 385, 893
Biggs A. D. et al., 2011, MNRAS, 413, 2314
Binney J., Tremaine S., 2008, Galactic Dynamics, 2nd edn. Princeton Univ. Press, Princeton, NJ
Blain A. W., Chapman S. C., Smail I., Ivison R., 2004, ApJ, 611, 725
Bothwell M. S. et al., 2010, MNRAS, 405, 219
Bothwell M. S. et al., 2012, preprint (arXiv:1205.1511)
Carilli C. L. et al., 2010, ApJ, 714, 1407
Casey C. M. et al., 2009, MNRAS, 399, 121
Casey C. M., Chapman S. C., Smail I., Alaghband-Zadeh S., Bothwell M. S., Swinbank A. M., 2011, MNRAS, 411, 2739
Chabrier G., 2003, PASP, 115, 763
Chapman S. C., Blain A. W., Ivison R. J., Smail I. R., 2003, Nat, 422, 695
Chapman S. C., Scott D., Windhorst R. A., Frayer D. T., Borys C., Lewis G. F., Ivison R. J., 2004a, ApJ, 606, 85
Chapman S. C., Smail I., Windhorst R., Muxlow T., Ivison R. J., 2004b, ApJ, 611, 732
Chapman S. C., Smail I., Blain A. W., Ivison R. J., 2004c, ApJ, 614, 671
Chapman S. C., Blain A. W., Smail I., Ivison R. J., 2005, ApJ, 622, 772
Chapman S. C., Blain A., Ibata R., Ivison R. J., Smail I., Morrison G., 2009, ApJ, 691, 560
Chapman S. C. et al., 2010, MNRAS, 409, L13
Copin Y. et al., 2001, in Combes F., Barret D., Thévenin F., eds, SF2A-2001: Semaine de l'Astrophysique Francaise, p. 289
Coppin K. et al., 2006, MNRAS, 372, 1621
Courteau S., 1997, AJ, 114, 2402
Daddi E., Cimatti A., Renzini A., Fontana A., Mignoli M., Pozzetti L., Tozzi P., Zamorani G., 2004, ApJ, 617, 746
Daddi E. et al., 2007, ApJ, 670, 156
Davé R., Finlator K., Oppenheimer B. D., Fardal M., Katz N., Kereš D., Weinberg D. H., 2010, MNRAS, 404, 1355
Dunlop J. S. et al., 2010, MNRAS, 408, 2022
Efstathiou G., 2000, MNRAS, 317, 697
Engel H. et al., 2010, ApJ, 724, 233
Erb D. K., Shapley A. E., Pettini M., Steidel C. C., Reddy N. A., Adelberger K. L., 2006, ApJ, 644, 813
Förster-Schreiber N. M. et al., 2009, ApJ, 706, 1364
Frayer D. T., Ivison R. J., Scoville N. Z., Yun M., Evans A. S., Smail I., Blain A. W., Kneib J., 1998, ApJ, 506, L7
Genzel R., Baker A. J., Tacconi L. J., Lutz D., Cox P., Guilloteau S., Omont A., 2003, ApJ, 584, L633
Genzel R. et al., 2006, Nat, 442, 786
Genzel R. et al., 2008, ApJ, 687, 59
Genzel R. et al., 2010, MNRAS, 407, 2091

González J. E., Lacey C. G., Baugh C. M., Frenk C. S., 2011, MNRAS, 413, 749
Greve T. R. et al., 2005, MNRAS, 359, 1165
Griffin M. J. et al., 2010, A&A, 518, L3
Hainline L. J., Blain A. W., Smail I., Alexander D. M., Armus L., Chapman S. C., Ivison R. J., 2011, ApJ, 740, 96
Harrison C. M. et al., 2012, preprint (arXiv:1205.1801)
Hayward C. C., Kereš D., Jonsson P., Narayanan D., Cox T. J., Hernquist L., 2011a, ApJ, 753, 159
Hayward C. C. et al., 2011b, in Treyer M., Wyder T., Neill J., Seibert M., Lee J., eds, ASP Conf. Ser. Vol. 440, UP2010: Have Observations Revealed a Variable Upper End of the Initial Mass Function? Astron. Soc. Pac., San Francisco, p. 369
Helou G., Soifer B. T., Rowan-Robinson M., 1985, ApJ, 298, L7
Hickox R. C. et al., 2012, MNRAS, 421, 284
Hughes D. H. et al., 1998, Nat, 394, 241
Hunter D. A., Rubin V. C., Swaters R. A., Sparke L. S., Levine S. E., 2005, ApJ, 634, 281
Ivison R. J. et al., 2007, MNRAS, 380, 199
Ivison R. J. et al., 2010, MNRAS, 402, 245
Ivison R. J., Papadopoulos P. P., Smail I., Greve T. R., Thomson A. P., Xilouris E. M., Chapman S. C., 2011, MNRAS, 412, 1913
Kennicutt R. C., Jr, 1998a, ARA&A, 36, 189
Kennicutt R. C., Jr, 1998b, ApJ, 498, 541
Kewley L. J., Groves B., Kauffmann G., Heckman T., 2006, MNRAS, 372, 961
Kneib J.-P., van der Werf P. P., Kraiberg Knudsen K., Smail I., Blain A., Frayer D., Barnard V., Ivison R., 2004, MNRAS, 349, 1211
Kovács A., Chapman S. C., Dowell C. D., Blain A. W., Ivison R. J., Smail I., Phillips T. G., 2006, ApJ, 650, 592
Krajnović D., Cappellari M., de Zeeuw P. T., Copin Y., 2006, MNRAS, 366, 787
Lehnert M. D., Nesvadba N. P. H., Tiran L. L., Di Matteo P., van Driel W., Douglas L. S., Chemin L., Bournaud F., 2009, ApJ, 699, 1660
Lilly S. J., Eales S. A., Gear W. K. P., Hammer F., Le Fevre O., Crampton D., Bond J. R., Dunne L., 1999, ApJ, 518, 641
Magdis G. E. et al., 2010, MNRAS, 409, 22
Magnelli B. et al., 2010, A&A, 518, L28
Magnelli B. et al., 2012, A&A, 539, A155
Matsuda Y. et al., 2011, MNRAS, 416, 2041
Mihos J. C., Hernquist L., 1996, ApJ, 464, 641
Miller N. A., Fomalont E. B., Kellermann K. I., Mainieri V., Norman C., Padovani P., Rosati P., Tozzi P., 2008, ApJS, 179, 114
Narayanan D., Cox T. J., Hayward C. C., Younger J. D., Hernquist L., 2009, MNRAS, 400, 1919
Neri R. et al., 2003, ApJ, 597, L113
Nesvadba N. P. H., Lehnert M. D., De Breuck C., Gilbert A. M., van Breugel W., 2008, A&A, 491, 407
Noeske K. G. et al., 2007, ApJ, 660, L43
Oliver S. J. et al., 2012, preprint (arXiv:1203.2562)
Riechers D. A., Hodge J., Walter F., Carilli C. L., Bertoldi F., 2011a, ApJ, 739, L31
Riechers D. A. et al., 2011b, ApJ, 733, L11
Sakamoto K. et al., 2008, ApJ, 684, 957
Salpeter E. E., 1955, ApJ, 121, 161
Sanders D. B., Mirabel I. F., 1996, ARA&A, 34, 749
Schaye J., Aguirre A., 2005, in Hill V., François P., Primas F., eds, Proc. IAU Symp. 228, From Lithium to Uranium: Elemental Tracers of Early Cosmic Evolution. Cambridge Univ. Press, Cambridge, p. 557
Shapiro K. L. et al., 2008, ApJ, 682, 231
Smail I., Ivison R. J., Blain A. W., 1997, ApJ, 490, L5
Smail I., Chapman S. C., Blain A. W., Ivison R. J., 2004, ApJ, 616, 71
Springel V., Di Matteo T., Hernquist L., 2005a, MNRAS, 361, 776
Springel V. et al., 2005b, Nat, 435, 629
Steidel C. C., Shapley A. E., Pettini M., Adelberger K. L., Erb D. K., Reddy N. A., Hunt M. P., 2004, ApJ, 604, 534
Swinbank A. M., Smail I., Chapman S. C., Blain A. W., Ivison R. J., Keel W. C., 2004, ApJ, 617, 64
Swinbank A. M. et al., 2005, MNRAS, 359, 401
Swinbank A. M., Chapman S. C., Smail I., Lindner C., Borys C., Blain A. W., Ivison R. J., Lewis G. F., 2006, MNRAS, 371, 465
Swinbank A. M. et al., 2008, MNRAS, 391, 420
Swinbank A. M. et al., 2010a, MNRAS, 405, 234
Swinbank A. M. et al., 2010b, Nat, 464, 733
Tacconi L. J. et al., 2006, ApJ, 640, 228
Tacconi L. J. et al., 2008, ApJ, 680, 246
Takata T., Sekiguchi K., Smail I., Chapman S. C., Geach J. E., Swinbank A. M., Blain A., Ivison R. J., 2006, ApJ, 651, 713
Tamura Y. et al., 2009, Nat, 459, 61
Tecza M. et al., 2004, ApJ, 605, L109
van Dokkum P. G., Kriek M., Rodgers B., Franx M., Puxley P., 2005, ApJ, 622, L13
Veilleux S., Kim D., Sanders D. B., 2002, ApJS, 143, 315
Wardlow J. L. et al., 2011, MNRAS, 415, 1479
Weiß A. et al., 2009, ApJ, 707, 1201

This paper has been typeset from a TEX/LATEX file prepared by the author.